EVALUATION OF FLOW BEHAVIOR AROUND AN AIRFOIL BODY

A Thesis Report Submitted
in partial fulfillment of the requirements for
the award of degree of

MASTER OF ENGINEERING
IN
CAD CAM & ROBOTICS

Submitted by

Aman Sharma
Roll No.: 801081033

Under the Guidance of

Mr. Satish Kumar
Department of Mechanical Engineering
Thapar University, Patiala.

Dr. Dwarika Nath Ratha
Department of Civil Engineering
Thapar University, Patiala.

DEPARTMENT OF MECHANICAL ENGINEERING
THAPAR UNIVERSITY
PATIALA-147004, INDIA.
July 2012

DECLARATION

I hereby declare that the work which is being presented in the dissertation work entitled, **"Evaluation of flow behavior around a airfoil body"**, in partial fulfillment of the requirements for the award of degree of Master of Engineering in Mechanical Engineering with specialization in **CAD/CAM & ROBOTICS** submitted in Mechanical Engineering Department of Thapar University, Patiala, is an authentic record of my own work carried out under the supervision of **Mr. Satish Kumar (Assistant Prof. MED) and Dr. Dwarika Nath Ratha (Assistant Prof. CED)** refers other researcher's works which are duly listed in the reference section.

The matter presented in this thesis has not been submitted for the award of any other degree of this or any other university.

Aman Sharma

Aman Sharma

This is to certify that the above statement made by the candidate is correct and true to the best of my knowledge.

Mr. Satish Kumar
Assistant Professor, MED
Thapar University, Patiala

Dr. Dwarika Nath Ratha
Assistant Professor, CED
Thapar university, Patiala

Counter signed by

Dr. Ajay Batish
Professor & head
Mechanical Engineering Department
Thapar University, Patiala

Dr. S.K. Mohapatra
Dean of Academic Affairs
Thapar University, Patiala

ACKNOWLEDGEMENTS

Words are often less to revels one's deep regards. With an understanding that work like this can never be the outcome of a single person, I take this opportunity to express my profound sense of gratitude and respect to all those who helped me through the duration of this work.

This work would not have been possible without the encouragement and able guidance of supervisor Mr. Satish Kumar and Dr. Dwarika Nath Ratha. Their enthusiasm and optimism made this experience both rewarding and enjoyable. Most of the novel ideas and solutions in this work are the result of our numerous stimulating discussions. Their feedback and editorial comments were also invaluable for the writing of this thesis. I am grateful to Dr. Maneek Kumar, Head of Department of Civil Engineering Department for providing me the facilities in the Department for the completion of my work.

I take pride of myself being son of ideal parents for their everlasting desire, sacrifice, affectionate blessings, and help, without which it would not have been possible for me to complete my studies.

I am also very grateful to my all friends and colleague for accompanying me during the most outstanding year of my life and standing by me in every situation.

I would like to thank to all the faculty members and employees of Mechanical Engineering Department, Thapar Univeristy, Patiala for their everlasting support.

Last but not least, I would like to thank God for all good deeds.

(Aman Sharma)

ABSTRACT

A wooden NACA 2415 airfoil is fabricated with four static pressure taps for measurement of surface pressure. The main objective of this investigation is to analyze the flow behavior around the airfoil body and to calculate the performance coefficients at Reynolds Number 1.04×10^5 and angle of attack from -5^0 to 18^0. The section-lift and drag coefficient for an asymmetric airfoil are obtained by analyzing the measured pressure distribution at pressure taps on the airfoil surface. The airfoil spans the test section. A U-tube manometer is used to monitor the surface pressure and provide a visual display of the dynamic changes associated with varying angle of attack. The experimental data for NACA 2415 from wind tunnel is validated with simulations computed in the software FLUENT. The airfoil is cambered and measures 100 mm. The lab data and simulations are performed at various angles of attack and lift and drag coefficients are computed. By plotting the curve L/D yields the most efficient airfoil angle of attack, found to be 17^0. Viscous model Spalart-Allmaras, k-ε and k-ω are used in FLUENT. The simulations in FLUENT yielded the best correlation to the experimental data with the viscosity model k-ω and had the overall best performance in determining the lift and drag coefficients. Lift increases as the angle of attack increases between -5 and +17 degrees and at +17 degrees maximum lift is generated. If the angle of attack is increased any further drag becomes the dominant factor and the wing enters the stall mode.

CONTENTS

Chapter		Item description	Page No.
		Contents	v-vii
		List of figures	viii-x
		List of tables	xi
		Abbreviations	xii
		Nomenclature and symbols	xii
1.		**Introduction**	
	1.1	Streamline body	1
	1.2	Bluff body	2
	1.3	Characteristics of airfoil	2
	1.4	Basic terminology of airfoil	3
	1.5	Different NACA profiles	5
	1.6	Different flow behavior	7
2.		**Literature review**	9
3.		**Experimental setup**	
	3.1	Design and fabrication of airfoil with methodology	21
	3.2	Description of experimental setup	24
	3.3	Procedure	25
	3.4	Observations	26
	3.5	Pressure coefficient	26
	3.6	Lift and pressure drag	27

3.6.1 Normal pressure force 27

3.6.2 Pressure drag 28

3.7 Lift and drag coefficient 29

3.8 Results 30

3.8.1 Velocity distribution 30

3.8.2 Lift and drag forces 31

4. **Numerical Evaluation of airfoil**

4.1 Background 34

4.2 Approach 34

4.2.1 Prepare geometric model 34

4.2.2 Meshing 35

4.2.3 Setting boundary conditions 36

4.2.4 Setting up FLUENT 37

4.2.4.1 Viscosity models 37

4.3 Results and discussions 37

4.3.1 Qualitative results 38

4.3.2 Performance coefficients 44

4.3.3 Pressure distribution 46

4.3.4 Surface flow visualization on airfoil surface 49

5. **PROTOTYPING**

5.1 Introduction 50

5.2 Geometric modeling 50

5.3 Meshing 51

5.4 Setting up fluent 52

5.5 Results 52

5.5.1 Different contour outputs 52

5.5.2 Performance coefficients 55

6. **Conclusion and future scope** 57

6.1 Conclusion 57

6.2 Future Scope 57

References 58

LIST OF FIGURES

Fig. No.	Item description	Page No.
1.1	Flow around a nicely streamlined body in a wind tunnel.	1
1.2	Bluff bodies	2
1.3	Characteristics of airfoil body	3
1.4	Comparison of NACA 4-digit airfoils of 6, 12, and 18% thicknesses.	6
1.5	Comparison of uncambered and cambered NACA 4-digit airfoils.	6
1.6	Conventional and Laminar flow airfoils	7
1.7	Turbulent vs. Laminar Boundary Flow	8
3.1	Fabricated airfoil body	23
3.2	Wind tunnel set up at fluid mechanics lab (Thapar University).	24
3.3	Close view of test section with airfoil	25
3.4	Normal pressure force on an airfoil surface.	27
3.5	Pressure regions on an airfoil	28
3.6	Component of airfoil	29
3.7	Velocity distributions along vertical position of Prandtl-Pitot tube.	31
3.8	Coefficient of lift and drag Vs angle of attack	32
3.9	Lift to drag ratio (L/D) Vs Angle of attack (AoA)	33
4.1	different mesh set ups for the CFD simulation	35
4.2	Velocity contour (-5^0 Angle of attack and viscosity model S-A).	38
4.3	Velocity contour (-5^0 Angle of attack and viscosity model k-ε).	38
4.4	Velocity contour (-5^0 Angle of attack and viscosity model k-ω).	38
4.5	Velocity contour (0^0 Angle of attack and viscosity model S-A).	39
4.6	Velocity contour (0^0 Angle of attack and viscosity model k-ε).	39
4.7	Velocity contour (0^0 Angle of attack and viscosity model k-ω).	39

4.8	Velocity contour (5^0 Angle of attack and viscosity model S-A).	40
4.9	Velocity contour (5^0 Angle of attack and viscosity model k-ε).	40
4.10	Velocity contour (5^0 Angle of attack and viscosity model k-ω).	40
4.11	Velocity contour (10^0 Angle of attack and viscosity model S-A).	41
4.12	Velocity contour (10^0 Angle of attack and viscosity model k-ε).	41
4.13	Velocity contour (10^0 Angle of attack and viscosity model k-ω).	41
4.14	Velocity contour (15^0 Angle of attack and viscosity model S-A).	42
4.15	Velocity contour (15^0 Angle of attack and viscosity model k-ε).	42
4.16	Velocity contour (15^0 Angle of attack and viscosity model k-ω).	42
4.17	Velocity contour (18^0 Angle of attack and viscosity model S-A).	43
4.18	Velocity contour (18^0 Angle of attack and viscosity model k-ε).	43
4.19	Velocity contour (18^0 Angle of attack and viscosity model k-ω).	43
4.20	Coefficient of lift Vs Angle of Attack.	44
4.21	Coefficient of drag Vs Angle of Attack.	44
4.22	Coefficient of lift and drag Vs Angle of Attack.	45
4.23	Lift/Drag ratios Vs Angle of Attack.	45
4.24	Pressure coefficient Vs X/C at Angle of Attack 0^0.	46
4.25	Pressure coefficient Vs X/C at Angle of Attack 6^0	47
4.26	Pressure coefficient Vs X/C at Angle of Attack 15^0.	47
4.27	Pressure coefficient Vs X/C at Angle of Attack $\alpha= 0^0$, 6^0 and 15^0. For_NACA_2415	48
4.28	Separation and reattachment points are shown on the airfoil surface at attack angles, $\alpha=0^0$, 6^0 and 15^0 respectively.	49
5.1	Meshing of the Prototype (NACA 2415)	51
5.2	Velocity contour (-5^0 Angle of attack and viscosity model k-ω).	52
5.3	Velocity contour (0^0 Angle of attack and viscosity model k-ω).	53

5.4	Velocity contour (5^0 Angle of attack and viscosity model k-ω).	53
5.5	Velocity contour (10^0 Angle of attack and viscosity model k-ω).	53
5.6	Velocity contour (15^0 Angle of attack and viscosity model k-ω).	54
5.7	Velocity contour (17^0 Angle of attack and viscosity model k-ω).	54
5.8	Velocity contour (18^0 Angle of attack and viscosity model k-ω).	54
5.9	Lift coefficient Vs Angle of Attack	55
5.10	Drag coefficient Vs Angle of Attack	55
5.11	Lift and Drag coefficients Vs Angle of Attack	56
5.12	Lift to Drag (L/D) ratio Vs Angle of Attack.	56

LIST OF TABLES

Table No.	Item description	Page No.
3.1	Upper and lower surface coordinates of airfoil body.	23
3.2	Specifications of the fabricated airfoil.	23
3.3	Values of velocity distribution along vertical position of Prandtl-Pitot tube.	30
3.4	Data obtained from the wind tunnel testing.	32
4.1	Different type of mesh ups.	36
5.1	Specifications of the prototype model.	51
5.2	Parameters used for meshing.	52

ABBREVATIONS

CFD	Computational fluid dynamics
NACA	National Advisory Committee For Aeronautics
RANS	Reynolds- averaged Navier stroke
DNS	Direct Navier stroke
S-A	Spallart-allmaras

NOMENCLATURE AND SYMBOLS

α	Angle of attack
C_L	Coefficient of lift
C_D	Coefficient of drag
L	Lift force
D	Drag force
ds	a Differential segment of the airfoil surface
C	chord length
C_P	Pressure coefficient
C_{PU}	Upper pressure coefficients
C_{PL}	Lower pressure coefficients
C_x	x force coefficient
C_z	z force coefficients
P_∞	free stream pressure
P_T	free stream total pressure
ρ	density
U_∞	free stream velocity

CHAPTER-1

INTRODUCTION

1.1 Streamline Body

The shape of many objects moving through air or water is designed in such a way that friction can be reduced between the objects and water or air the shape of the body is called streamlined body.

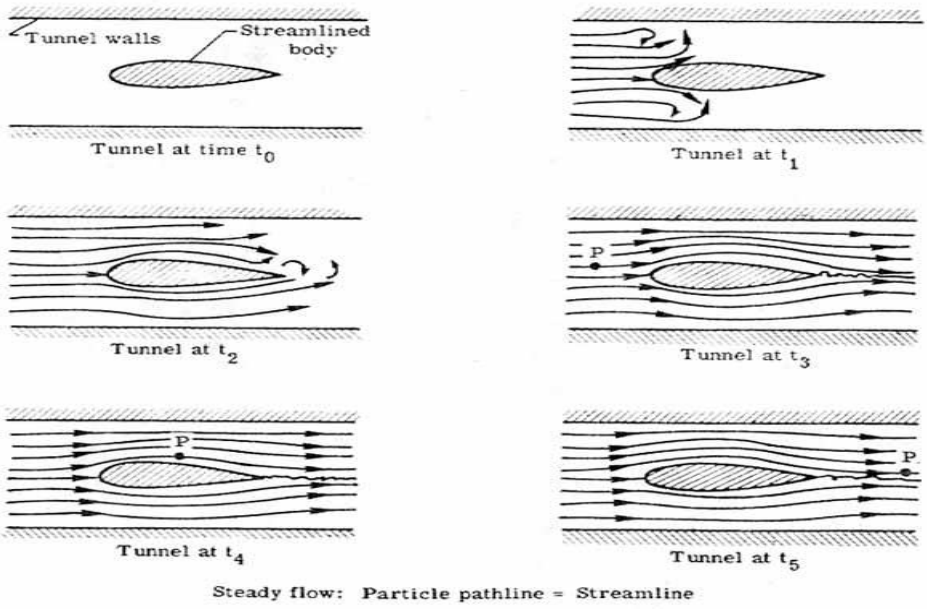

Figure-1.1

Figure-1 shows unsteady and steady flow around a nicely "streamlined" body in a wind tunnel. At time t0 the tunnel is not running and no air is flowing. At time t1 the tunnel is started and air begins flowing about the body.

Streamlining is the shaping of an object, such as an aircraft body or wing, to reduce the amount of drag or resistance to motion through a stream of air. A curved shape allows air to flow smoothly around it. A flat shape fights air flow and causes more drag or resistance. Streamlining reduces the amount of resistance and increases lift. To produce

less resistance, the front of the object should be well rounded and the body should gradually curve back from the midsection to a tapered rear section

1.2 Bluff Body

Bluff body looks like a brick, a cylinder, or an airfoil at large angles of attack or A body having a broad, flattened front, as in some reentry vehicles. "Bluff bodies" are characterized by a more or less precocious separation of the boundary layer from their surface and by wakes having significant lateral dimensions and normally unsteady velocity fields. For these bodies no simplified mathematical treatment is usually possible and the forces acting on them may be evaluated either from the solution of the complete Navier-Stokes equations or from the results of ad hoc experiments. The type of flow occurring is defined not only by the shape of the body but also by its orientation to the flow and any aerodynamic body may become a bluff body for certain free-stream directions.

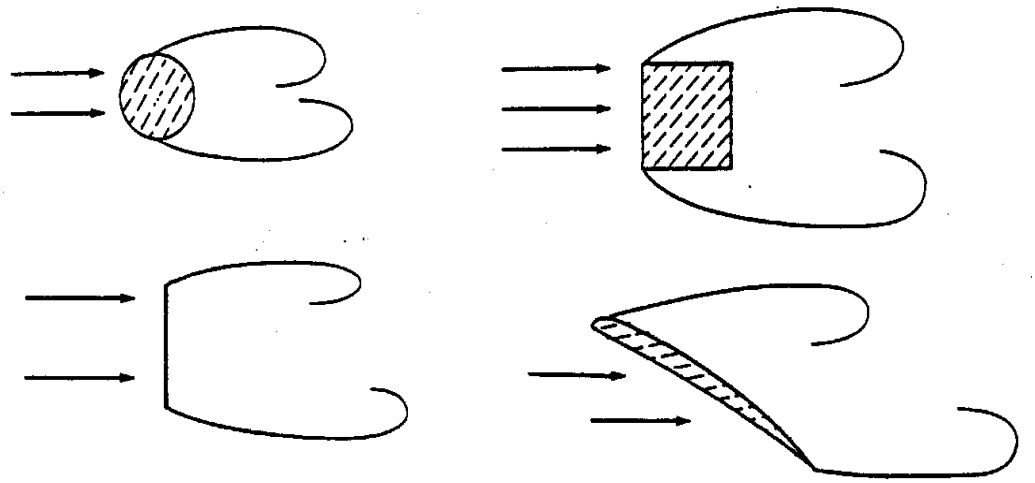

Figure-1.2 (Bluff bodies)

1.3 Airfoil

An airfoil is the shape of a wing or blade (of a propeller, rotor or turbine) or sail. An airfoil shaped body moved through a fluid produces an aerodynamic force. The component of this force perpendicular to the direction of motion is called lift. The

component parallel to the direction of motion is called drag. Subsonic flight airfoils have a characteristic shape with a rounded leading edge, followed by a sharp trailing edge, often with asymmetric camber. Foils of similar function designed with water as the working fluid are called hydrofoils. Fig no.-3 shows the different parameters of the airfoil.

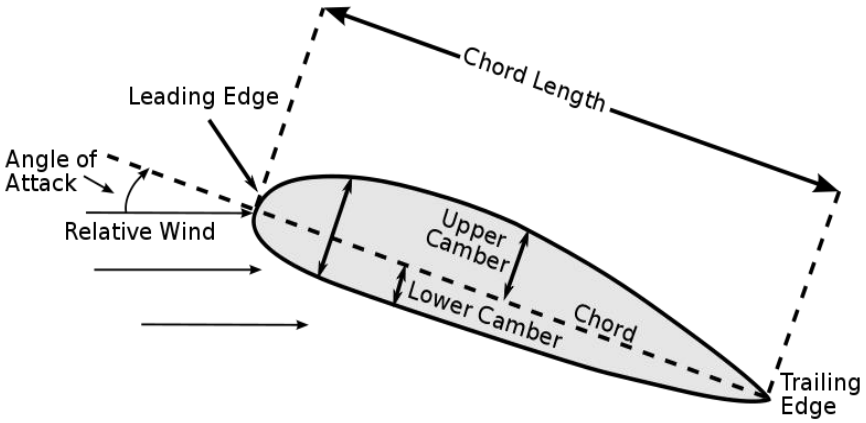

Figure-1.3

Chord length: The cord length is a straight line connecting the leading and trailing edges of the airfoil.

Leading edge: The leading edge is the part of the airfoil that first contacts the air. Alternatively it is the foremost edge of an airfoil section.

Trailing edge: The trailing edge of an aerodynamic surface such as a wing is its rear edge, where the airflow separated by the leading edge rejoins.

Angle of attack: Angle of attack (AOA, α) is a term used in fluid dynamics to describe the angle between a reference line on a lifting body (often the chord line of an airfoil).

The lift on an airfoil is primarily the result of its angle of attack and shape. When oriented at a suitable angle, the airfoil deflects the oncoming air, resulting in a force on the airfoil in the direction opposite to the deflection. This force is known as aerodynamic force and can be resolved into two components: Lift and drag. Most foil shapes require a positive angle of attack to generate lift, but cambered airfoils can generate lift at zero angle of

attack. This "turning" of the air in the vicinity of the airfoil creates curved streamlines which results in lower pressure on one side and higher pressure on the other. This pressure difference is accompanied by a velocity difference, via Bernoulli's principle, so the resulting flow field about the airfoil has a higher average velocity on the upper surface than on the lower surface. The lift force can be related directly to the average top/bottom velocity difference without computing the pressure by using the concept of circulation and the Kutta-Joukowski theorem.

1.4 Basic Terminology Of Airfoil

The various terms related to airfoils are defined below:

- The suction surface (upper surface) is generally associated with higher velocity and thus lower static pressure.
- The pressure surface (lower surface) has a comparatively higher static pressure than the suction surface. The pressure gradient between these two surfaces contributes to the lift force generated for a given airfoil.

The geometry of the airfoil is described with a variety of terms.

A key characteristic of an airfoil is its chord. We thus define the following concepts:

- The leading edge is the point at the front of the airfoil that has maximum curvature.
- The trailing edge is defined similarly as the point of maximum curvature at the rear of the airfoil.
- The chord line is a straight line connecting the leading and trailing edges of the airfoil.
- The chord length, or simply chord, c, is the length of the chord line and is the characteristic dimension of the airfoil section.

The shape of the airfoil is defined using the following concepts:

- The mean camber line is the locus of points midway between the upper and lower surfaces. Its exact shape depends on how the thickness is defined;
- The thickness of an airfoil varies along the chord. It may be measured in either of two ways:
    - Thickness measured perpendicular to the camber line. This is sometimes described as the "American convention";
    - Thickness measured perpendicular to the chord line. This is sometimes described as the "British convention".

Two key parameters to describe an airfoil's shape are its maximum thickness (expressed as a percentage of the chord), and the location of the maximum thickness point (also expressed as a percentage of the chord).

Finally, important concepts used to describe the airfoil's behavior when moving through a fluid are:

- The aerodynamic center which is the chord-wise length about which the pitching moment is independent of the lift coefficient and the angle of attack.
- The center of pressure which is the chord-wise location about which the pitching moment is zero.

1.5 Different NACA(National Advisory Committee For Aeronautics) Profiles

The early NACA airfoil series, the 4-digit, 5-digit, and modified 4-/5-digit, were generated using analytical equations that describe the camber (curvature) of the mean-line (geometric centerline) of the airfoil section as well as the section's thickness distribution along the length of the airfoil. Later families, including the 6-Series, are more complicated shapes derived using theoretical rather than geometrical methods. Before the National Advisory Committee for Aeronautics (NACA) developed these series, airfoil design was rather arbitrary with nothing to guide the designer except past experience with known shapes and experimentation with modifications to those shapes. Different NACA airfoil profiles are shown as below:

- The comparison between the profiles was taken on the basis of thickness parameter i.e. (t/c):

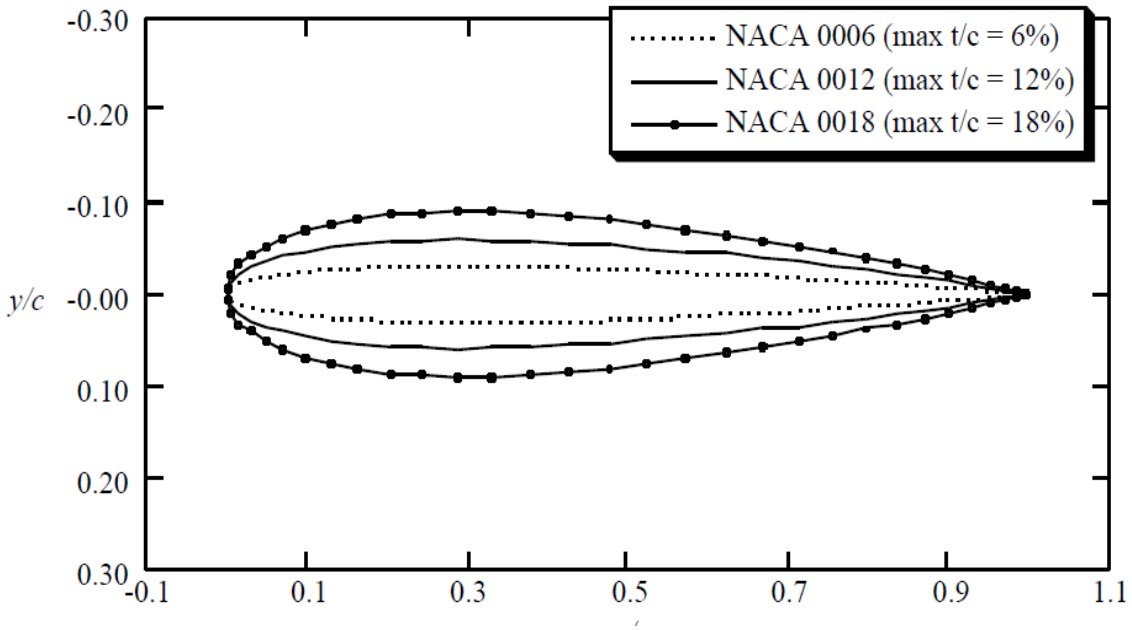

Figure-1.4(Comparison of NACA 4-digit airfoils of 6, 12, and 18% thicknesses)

- The comparison between the profile was taken on the basis of shape i.e. (symmetrical or asymmetrical):

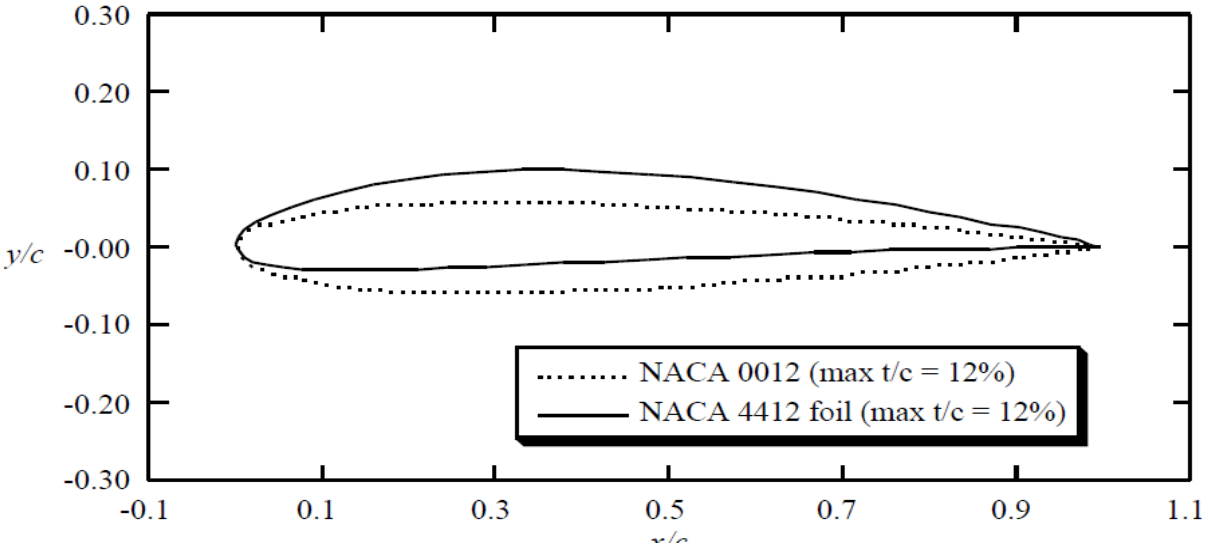

Figure-1.5 (Comparison of uncambered and cambered NACA 4-digit airfoils)

- Conventional and Laminar flow airfoils:

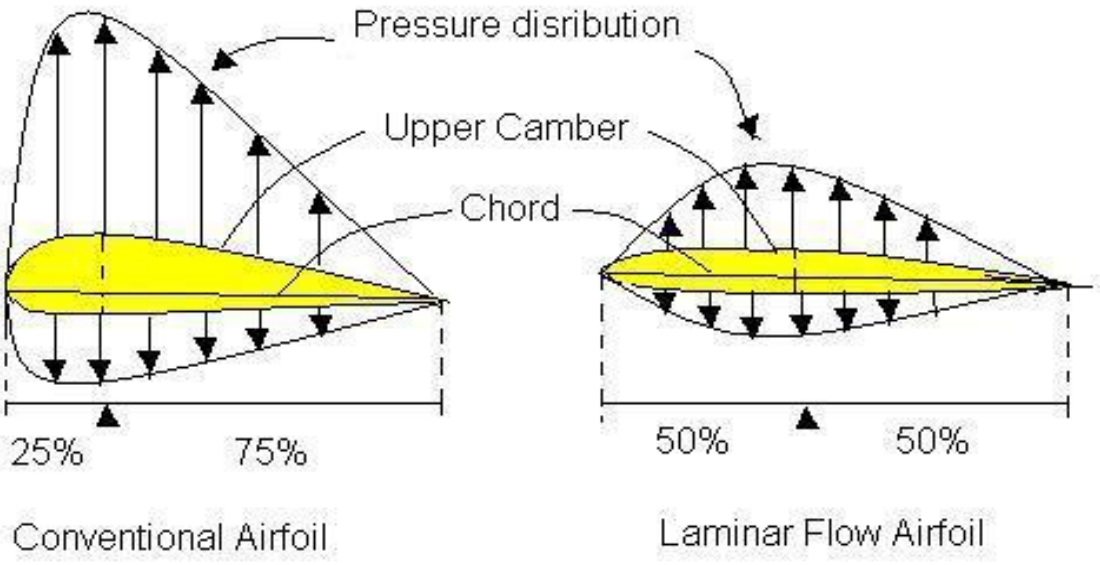

Figure-1.6

1.6 Different Flow Behavior

Laminar flow is characterized by layers, or laminas, of air moving at the same speed and in the same direction. No fluid is exchanged between the laminas and the flow need not be in a straight line. The closer the laminas are to the airfoil surface the slower they move. For an ideal fluid the flow follows the curved surface smoothly, in laminas. In turbulent flow, the streamlines or flow patterns are disorganized and there is an exchange of fluid between these areas. Momentum is also exchanged such that slow moving fluid particles speed up and fast moving particles give up their momentum to the slower moving particles and slow down themselves. All or nearly all fluid-flow displays some degree of turbulence.

In figure 7 the laminar boundary layer in the upper photo is shown separating from the crest of the convex surface, while the turbulent boundary layer in the second photo remains attached longer with the point of separation occurring further downstream.

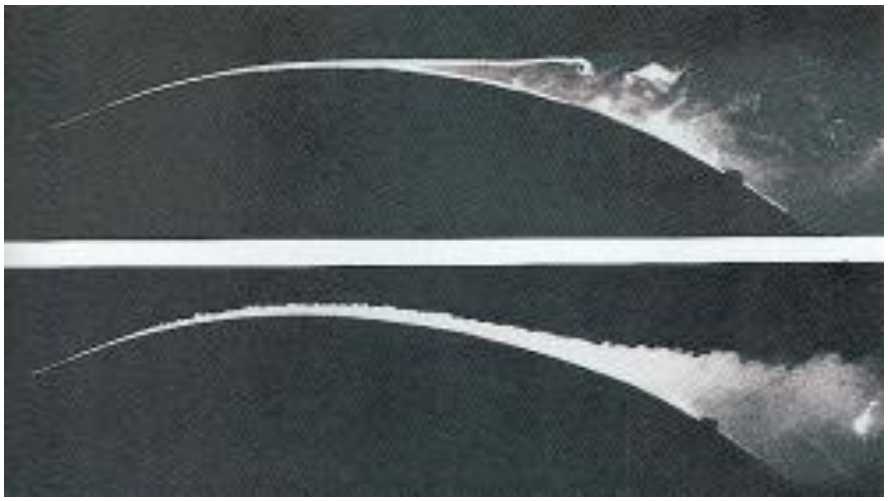

Figure-1.7 Turbulent vs. Laminar Boundary Flow

The Reynolds number is an important value for the behavior of the flow, and especially the boundary layer. Flows with the same Reynolds number behave similar. This number can be calculated by the exact formula. If medium accuracy is sufficient, the Reynolds number can be approximately calculated by the equation (i) given below:

$$Re = v \times l \times 70000 \qquad (1.1)$$

where: "v" is flight speed

"l" is chord length in m.

70000 constant value for air (s/m^2).

The Reynolds number is based on a length, which is usually the chord length of an airfoil (in two dimensions) or the chord length of a wing. Because the chord length of a wing may vary from root to tip, a mean aerodynamic chord length is used to define the Reynolds number for a wing.

CHAPTER-2

LITERATURE SURVEY

The literature review has been conducted to focus on the following areas:

Guilmineau et al. (1997) discussed the computation of the time-mean, turbulent, two-dimensional incompressible viscous flow past an airfoil at fixed incidence. A new physically consistent method is presented for the reconstruction of velocity fluxes which arise from discrete equations for the mass and momentum balance. This closure method for fluxes makes possible the use of a cell-centred grid in which velocity and pressure unknowns share the same location, while circumventing the occurrence of spurious pressure modes. The influence of several turbulent models is investigated. The models involve either an algebraic eddy viscosity or determine the eddy viscosity from transport equations. Calculations performed have also indicated that the grid independence should be verified rather on velocity characteristics than on pressure data which are easily made grid-free. The importance of grid effects, moreover, increases when the nominal Reynolds number increases, while the transition phenomenon is the most critical physical difficulty which prevents a fully automatic flow prediction.

S. B. Hazra et al. (1997) they optimized airfoils at ultra-low Reynolds numbers. These investigations are carried out to understand the aerodynamic issues related to the low speed and micro scale air vehicle design and performance. The optimization method used is based on simultaneous pseudo-time stepping in which stationary states are obtained by solving the preconditioned pseudo-stationary system of equations representing the state, co state and design equations. Design examples of airfoils of different thicknesses at Mach numbers between the range of 0.25 to 0.3 and at Reynolds numbers below 15000 are presented.

N. Ahmed et al. (1998) studied the Numerical simulation of flow past airfoils is important in the aerodynamic design of aircraft wings and turbo-machinery components. These lifting devices often attain optimum performance at the condition of onset of

separation. Therefore, separation phenomena must be included if the analysis is aimed at practical applications. Consequently, in the present study, numerical simulation of steady flow in a linear cascade of NACA 0012 airfoils is accomplished with control volume approach. The flow field is determined by solving two-dimensional incompressible Navier-Stokes equations while the effects of turbulence are accounted for by the *k--E* model. Boundary layer developed at the suction and the pressure surfaces of the airfoil is investigated together with relevant pressure contours for different angles of attack and solidity. Separation point at the airfoil surface is predicted at high angles of attack. Pressure, lift and drag coefficients are computed and the results are compared with the predictions of isolated single NACA 0012 airfoil as well as the data available in the literature. However, the leading edge rotation is also introduced to determine the effect of leading edge rotation on stall inception of isolated airfoil. It is found that increase in solidity increases the angle of attack at which separation occurs and pressure, lift and drag coefficients are highly influenced by the angle of attack and the solidity.

T. K. Sengupta et al. (1999) unsteady flow past a NACA 0015 aerofoil is investigated for moderate Reynolds numbers at high angles of attack by solving the full 2-D Navier}Stokes equations with and without the presence of free-stream turbulence (FST). The investigation focuses on the by-pass mode of transition usually encountered in turbo-machinery and wind engineering where the flow field around a bluff-body can experience very high levels of FST. In this study, a 5% level of FST is considered. While FST is all-pervasive, its effect has not been studied at all theoretically. Here, this has been made possible by proposing a new model for FST based on a moving-average time-series and using it for long-time computation of the Navier} Stokes equations. The statistics of the modeled FST follows the statistics of a specific wind tunnel. The use of this model in conjunction with higher order up-winding for the convection term to model the vorticity dynamics, gives the solution a very high degree of accuracy in the by-pass transitional flow regime. The present study is relevant for understanding the implications of reduced order modeling proposed for aero-elastic studies. The numerical results view the solution of the Navier} Stokes equations not only as the output of a dynamical system in the presence of stochastic noise (FST), but which also produces the intermittency factor in

and around the aerofoil dominated by differing pressure gradient and unsteady effects. The last attribute is also a novel feature of the present study and is relevant to bluff-body flow fields. The computed flow field shows that the flow achieves a statistical stationarity even though the overall flow is chaotic and aperiodic.

Kunz et al. (2000) studied the program at Arizona State University (ASU) consisted of complementary experimental, computational and flight test elements that examined the aerodynamics of Micro Aerial Vehicles (MAV's). All these components supported the actual design of our MAV, called MAVRIC (Micro Aerial Vehicle Research Initiative and Competition) and which competed for two years against other university teams. MAVs are characterized by low operating chord Reynolds numbers and thus present challenges in viscous aerodynamics. Our studies focused on the effects on performance of different wing body-juncture and wing-tip designs. MAV aerodynamics is strongly affected by the wing-tip vortices which extend over a significant amount of span. Blending the wing and fuselage and adding winglets provided a reduction in the extent of these vortices as well as a refocusing of them away from the lifting surface.

Bouhadji and Braza (2001) identified the successive stages in the transition of unsteady viscous transonic flow around an airfoil is carried out by solving the time-dependent Navier–Stokes equations for a compressible fluid in two-dimensional approach. The numerical simulation is carried out at the Mach number range (0.2–0.98). At a fixed Reynolds number (Re =10,000), it is found that this flow undergoes the following four transition steps: It remains steady up to the Mach number values (0.2–0.35) and afterwards it develops spontaneously, without any imposed artificial perturbation, an inherent unsteadiness corresponding to a near-wake von Karman instability, in the Mach number range (0.35–0.9). It is found that there exists a critical Mach number between the values (0.90–0.95) for which the flow returns to a steady-state. the flow is found to be governed by two instability processes in the Mach number range (0.75–0.8), where, apart from the von Karman mode (mode I), a lower frequency mode II appears, due to the formation of weakly supersonic alternating zones in the region upstream of the aerofoil, related to the buffeting phenomenon. A triple role played by the increasing

compressibility effects to trigger the instability processes, to maintain and to inhibit them in the transonic flow regime is therefore analyzed.

Hafez and Wahba (2002) presented a hierarchical formulation for steady inviscid and viscous transonic flows over airfoils and wings. They compared the result to available solutions of standard Navier–Stokes equations for laminar flows. Two and three dimensional laminar transonic flows are simulated and the results are encouraging. In principle, the method is applicable to the simulation of turbulent flows as well, using available turbulence models. In the viscous flow region, the components of velocity are governed by convection/diffusion equations and are solved in a segregated manner. An artificial time dependent term is added to each equation. Upwind differences are used for the convection terms. The artificial viscosity introduced via this discretization affects the accuracy of the calculations but it is necessary for numerical stability, particularly for high Reynolds number flows. Line relaxation, marching with the main flow direction, is employed to calculate the corrections. A tri-diagonal solver is needed to solve for the unknowns along a grid line as normal to the flow direction as possible. At different Mach numbers and Reynold numbers they calculated results on different angle of attacks and find the present calculations are in good agreement with results of their reference and with Overflow results based on standard Navier–Stokes equations.

Sanjay Mittal et al. (2002) performed the computational analysis for two-dimensional flow past stationary NACA 0012 airfoil is carried out with progressively increasing and decreasing angles of attack. The incompressible, Reynolds averaged Navier–Stokes equations in conjunction with the Baldwin–Lomax model, for turbulence closure, are solved using stabilized finite element formulations. Beyond a certain angle of attack the flow stalls with a sudden loss of lift and increase in drag. Hysteresis in the aerodynamic coefficients is observed for a small range of angles of attack close to the stall angle. This is caused by the difference in the location of the separation point of the flow on the upper surface of the airfoil during the increasing and decreasing angles of attack. Hysteresis in the flow has been observed close to the stall. With the increasing angle of attack, stall occurs at 19 while for the decreasing angle it occurs at 17. The ability of the flow to

remember its past history is responsible for its hysteretic behavior. Close to the stall the movement of the separation point with angle of attack is relatively slow with the increasing angle while it is quite abrupt with the decreasing angle. For the same angle of attack, in the hysteresis loop, the flow obtained with the decreasing angle of attack is associated with larger unsteadiness, lower lift and higher drag while the one with increasing angle results in higher lift and lower drag.

James Baeder et al. (2004) give the efficient prediction of helicopter rotor performance, vibratory loads, and aero-elastic properties still relies heavily on the use of comprehensive analysis codes by the rotorcraft industry. These comprehensive codes utilize look-up tables to provide two-dimensional aerodynamic characteristics. Typically these tables are comprised of a combination of wind tunnel data, empirical data and numerical analyses. The potential to rely more heavily on numerical computations based on Computational Fluid Dynamics (CFD) simulations has become more of a reality with the advent of faster computers and more sophisticated physical models. The ability of five different CFD codes applied independently to predict the lift, drag and pitching moments of rotor airfoils is examined for the SC1095 airfoil, which is utilized in the UH-60A main rotor. Extensive comparisons with the results of ten wind tunnel tests are performed. These CFD computations are found to be as good as experimental data in predicting many of the aerodynamic performance characteristics. Four turbulence models were examined (Baldwin-Lomax, Spalart-Allmaras, Menter SST, and k-ω)

T. Nakano et al. (2006) discussed the flow characteristics on and around an airfoil at moderate Reynolds number are studied to understand the generation mechanism of tonal noise from a symmetrical airfoil NACA0018 in a uniform flow. The separation and reattachment of the flow on the airfoil surface are evaluated from the liquid-crystal visualization and the velocity fields across the boundary layers over the airfoil are measured by particle image velocimetry (PIV). These results indicate that the separation and reattachment points of laminar boundary layers over the airfoil move along the airfoil surface, depending on the angle of attack variations. When the airfoil is inclined at a small attack angle to meet with the condition of tonal noise generation, the boundary

layer on the pressure surface experiences the separation along the surface and reattaches near the trailing edge of the airfoil. Then, the periodic vortex structure is generated over the pressure surface near the trailing edge, which is followed by the formation of periodic vortex shedding in the airfoil wake. With further increase in attack angle, the flow over the suction surface separates near the leading edge of the airfoil and the boundary layer on the pressure surface keeps fully attached flows on the airfoil surface, resulting in the disappearance of tonal noise.

J.J. Wang et al. (2006) performed Wind tunnel experiments were conducted to investigate the effects of divergent trailing edges and Gurney flaps on a supercritical airfoil at a Mach number M = 0.7 and a Reynolds number Re = 3.15 × 105 based on the airfoil chord length. The effects of Gurney flaps on a divergent trailing edge airfoil were also studied. Four Gurney flaps with heights h = 0.5%, 1.0%, 1.5% and 2.0% chord length, respectively, were employed in this investigation. The results revealed that, in comparison with the divergent trailing edge, the Gurney flaps had significant effects on improving the aerodynamic characteristics of the tested supercritical airfoil, and even on the airfoil with divergent trailing edge. When the Gurney flaps were utilized, the lift coefficient, maximum lift coefficient and the maximum lift-to-drag ratio of both supercritical and divergent trailing edge airfoils were greatly increased. Moreover, the installation of Gurney flaps will increase wave drag and base-pressure drag, but at the same time, the pressure on the lower surface of the airfoil was increased which led to an increased rear-body loading, and the position of the shock on the upper surface was greatly shifted backward, the supersonic region is thus enlarged, which led to an increased suction. Both the increments of pressure on the lower surface and suction on the upper surface resulted in a total lift increase. As the lift did not increase with the drag linearly, the lift-to-drag ratio increase and aerodynamic characteristics improvement were obtained under some circumstances.

Lowson et al. (2007) experimented the tonal noise the self-induced discrete frequency noise generated by airfoils is investigated. It is heard from an aerofoil placed in streams at low Mach number flows when inclined at a small angle to the stream. Tonal noise is

largely dependent on the existence of a separation bubble close to the trailing edge of the aerofoil. The distinctive ``piercing whistle" or singing" tones radiated by the aerofoil are due to a coupling between the boundary layer and wake instabilities, where there exists a single resonance frequency. The frequency of the vortex-street in the wake is determined by the development of boundary-layer instability waves on the pressure surface of the aerofoil. A frequency prediction may be obtained by calculating the growth of spatially growing modes in the boundary layer. This differs from the classical approach which presumes a wake controlled phenomenon, predicting the frequencies by using a Strouhal number mechanism based on the wake thickness (similar to predicting the frequencies in the wake of a bluff body).

Nitin R. Kapania et al. (2008) characterized airfoil model for the fluid flow around airfoils, it is important to define air-foils geometrically and to acquaint ourselves with the nomenclature with which they are characterized. Airfoil shapes are commonly characterized with a numbering system originally defined by the National Advisory Committee for Aeronautics (NACA). This characterizing system defines airfoil shapes with a series of digits corresponding to non-dimensionalized airfoil properties. The number of digits used to describe an airfoil corresponds to the complexity of the airfoil. For this paper, they will only model four digit (4-series) airfoils to simplify the geometry of the airfoils we wish to analyze. In 4-series airfoils, the profile is defined as follows:

- The first digit describes the maximum camber as a percentage of the chord length. The maximum camber is the maximum distance between the chord and mean camber line along the axis of the chord.
- The second digit indicates the position of the maximum camber in tenths of the chord.
- The last two digits provide the maximum thickness of the airfoil as a percent of the chord length.

Junqiang et al. (2008) studied an aerodynamic characteristic’s of a low-drag high-speed nature laminar flow (NLF) airfoil for business airplanes in the TST27 wind tunnel. In an attempt to reduce the errors of measurement and improve its accuracy in high-speed flight, some nonintrusive measurement different techniques, such as the quantitative

infrared thermography (IRT), the digital particle imaging velocimetry (PIV), and the shadowgraphy, are applied to obtain precise data about transition locations, separation on trailing edges, and lift/drag characteristics. They had performed an experiment to determine the aerodynamic characteristics of the airfoil including lift, drag, and separation transition. They results that the high-speed nature laminar flow airfoil is triumphantly designed and manufactured. From $\alpha=-2^0$ to $\alpha=2^0$, it is in possession of a long laminar flow on the upper surface and a stable separated vortex on the trailing.

Moin et al. (2008) performed large-eddy simulation of turbulent flow separation over an airfoil and evaluate the effectiveness of synthetic jets as a separation control technique. The flow configuration consists of flow over an airfoil at Reynolds number of 896,000 based on the airfoil chord length and free stream velocity. A small slot across the entire span connected to a cavity inside the airfoil is employed to produce oscillatory synthetic jets. Detailed flow structures inside the synthetic-jet actuator and the synthetic-jet/cross-flow interaction are simulated using an unstructured-grid finite-volume large-eddy simulation solver. Simulated results are compared with the 2005 experimental data of Gilarranz et al., and qualitative and quantitative agreements are obtained for both uncontrolled and controlled cases. As in the experiment, the present large-eddy simulation confirms that synthetic-jet actuation effectively delays the onset of flow separation and causes a significant increase in the lift coefficient. Modification of the blade boundary layer due to oscillatory blowing and suction and its role in separation control is discussed.

Liu et al. (2008) had done experimental and numerical study for hydrodynamic characteristics of an oscillating hydrofoil. They report the experimental Particle Image Velocimetry (PIV) investigation and the corresponding numerical simulation results about the water flow over the oscillating hydrofoil and its unsteady dynamic characters. The experimental study focuses on the effect of mean angles of attack. The comparison between the PIV results and numerical prediction about the flow field using Fluent well demonstrates the capability of CFD on the simulation of the water flow around the pitching hydrofoil. The numerical results indicate that the forced oscillating frequencies

have evident effects on the flow separation and vortex shedding. The simulations about the hydrodynamic drag and lift coefficients were also performed.

Masoud Mirzaei et al. (2009) studied the characteristics of separated bubbles and unsteady features of flow fields around a glaze-iced airfoil are investigated. The airfoil was a natural laminar airfoil (NLF-0414) and the ice is considered as the glaze accretion. The experimental measurements were carried out using hot-wire anemometry at Reynolds number of 0.5×10^6 and angle of attack ranging from $0\circ$ to $6\circ$. In numerical calculations, N–S equations were adopted as governing equations and finite-volume technique was employed to solve the equations. Numerical calculations were performed at Reynolds numbers of 0.5×10^6 and 1×10^6. CFD results and experimental data indicated increasing in the bubble length with increasing in airfoil angle-of-attack**.** The CFD results show that the flow field with two-dimensional ice simulations consisted of a main primary clockwise re-circulating separation region enclosed by a shear layer and a small, counterclockwise re-circulating, and secondary separation region formed behind the intersection of the ice and airfoil. It was found that the primary separation bubble grew with increasing angle-of-attack. Vortex structures were observed in the aft of reattachment. The frequencies corresponding to the vortices decrease at the downstream of the reattachment location similar to the backward-facing step flow field. And finally, time-dependent CFD results show the low frequency oscillations of lift and moment coefficients near stall angle-of- attack.

Derksen and Rogalsky (2009) introduced an optimised airfoil parameterization for design. Numerical search for the optimum shape of an aerofoil is of great interest for aircraft and turbo machine designers. They anticipate that some parameterizations will be less suitable for describing the profile shape and may result in slower convergence times. Their paper will discuss a new airfoil parameterization, Bezier-PARSEC that was developed to extend and improve the typical Bezier parameterization found in use. This parameterization was found to fit the known shape of a wide range of existing airfoil profiles as well as resulting in accelerated convergence for aerodynamic optimization using Differential Evolution. They used three parameterization methods (Bezier, BP-

3333 and BP-3434) that were all capable of representing a wide range of airfoil shapes. The BP 3333 parameterization performed better, and certainly no worse than the Bezier parameterization for inverse design. Overall, then, BP 3333 is a definite improvement over the Bezier parameterization. It is more separable, is more closely linked to the aerodynamics of the shape, and has fewer parameters.

Srinath and Mittal (2010) introduced a continuous ad joint formulation is used to determine optimal airfoil shapes in unsteady viscous flows at $Re=1\times10^4$. The Reynolds number is based on the free-stream speed and the chord length of the airfoil. The airfoil is parameterized via a Non-Uniform Rational B-Spline (NURBS) curve. Three different objective functions are used to obtain optimal shapes: maximize lift, minimize drag and minimize ratio of drag to lift. The objective functions are formulated on the basis of time-averaged aerodynamic coefficients. The three objective functions result in diverse airfoil geometries. The resulting airfoils are thin, with the largest thickness to chord ratio being only 5.4%. The shapes obtained are further investigated for their aerodynamic performance. Maximization of time-averaged lift leads to an airfoil that produces more than six times more lift compared to the NACA 0012 airfoil. The excess lift is a consequence of the large peak and extended region of high suction on the upper surface and high pressure on the lower surface. Minimization of drag results in an airfoil with a sharp leading edge. The flow remains attached for close to 70% of the chord length. Minimization of the ratio's of drag to lift results in an airfoil with a shallow dimple on the upper surface. It leads to a fairly large value of the time-averaged ratio of lift to drag (~17.8). The high value is mostly achieved by a 447% increase in lift and 16% reduction in drag, compared to a NACA 0012 airfoil.

Dr.D.Ravindran et al. (2010) gives the Lift and Drag forces along with the angle of attack are the important parameters in a wind turbine system. These parameters decide the efficiency of the wind turbine. In this paper an attempt is made to study the Lift and Drag orces in a wind turbine blade at various sections and the effect of angle of attack on these forces. In this paper NACA 4420 airfoil profile is considered for analysis of wind turbine blade. The wind turbine blade is modeled and several sections are created from

root to tip. The Lift and Drag forces are calculated at different sections for angle of attack from 0^o to 12^o for low Reynolds number. The analysis showed that angle of attack of 5^o has high Lift/Drag ratio. The CFD analysis is also carried out at various sections of blade at angle of attack of 5^o. The pressure and velocity distributions are also plotted. The airfoil NACA 4420 is analyzed based on computational fluid dynamics to identify its suitability for its application on wind turbine blades and good agreement is made between results. The results demonstrate the pressure distribution over the airfoil. The pressure on the lower surface of the airfoil is greater than that of the incoming flow stream and as a result of that it effectively pushes the airfoil upward, normal to the incoming flow stream. On the other hand, the components of the pressure distribution parallel to the incoming flow stream tend to slow the velocity of the incoming flow relative to the airfoil, as do the viscous stresses. It could be observed that the upper surface on the airfoil experiences a higher velocity compared to the lower surface. By increasing the velocity at higher Mach numbers there would be a shock wave on the upper surface that could cause discontinuity.

Ogumaa et al. (2010) performed the experiment on the flow characteristics on and around an airfoil at moderate Reynolds number are studied to understand the generation mechanism of tonal noise from a symmetrical airfoil in a uniform flow. The separation and reattachment of the flow on the airfoil surface are evaluated from the liquid-crystal visualization and the velocity fields across the boundary layers over the airfoil are measured by particle image velocimetry (PIV). When the airfoil is inclined at a small attack angle to meet with the condition of tonal noise generation, the boundary layer on the pressure surface experiences the separation along the surface and reattaches near the trailing edge of the airfoil. Thus, the long separation bubbles are created on the airfoil and the bubble on the pressure surface is placed downstream near the trailing edge. The mean velocity measured by PIV indicates that the inflection in the velocity profile is found in the separation region and the turbulence intensity increases a bit upstream of the reattachment point, which are followed by the reattachment and the generation of turbulent boundary layer on the suction surface and the formation of periodic vortex structure on the pressure surface near the trailing edge of the airfoil at small attack angles.

Lee et al. (2011) worked on a low Reynolds number airfoil that was designed for applications in small horizontal axis wind turbines to achieve better start up and low wind speed performances. Their experiments were performed on the improved airfoil (AF300) in an open circuit wind tunnel at Reynolds numbers of 38,000, 75,000, 128,000 and 205,000. Pressure distributions were obtained over the surface of the airfoil and the lift and drag forces were measured with a dynamometer at different angles of attack, α. A CFD analysis was also performed to get additional information on the flow characteristics. Particle Image Velocimetry (PIV) together with smoke flow visualization were used to study the flow around the airfoil. At the Reynolds numbers of 75,000, 128,000 and 205,000, maximum lift coefficients of 1.72, 1.81 and 1.86 respectively were obtained at the stall angle of 14°. The lift coefficient increased from 0.41 to 1.05 at Re = 38,000 in the range of α= 0–18°, in which no stalling was documented. The results from PIV and smoke flow visualization showed that the flow stayed fully attached to the airfoil surface from Re as low as 56,000 at an angle of attack of 8° and maintained a fully attached flow up to 14° angle of attack for Re as low as 75,000.

CHAPTER-3

EXPERIMENTAL SETUP

3.1 Design and fabrication of an airfoil with methodology

As the airfoil used is NACA 2415 designed using the approach known as the NACA Four-Digit Series. According to this approach the first digit specifies the maximum camber (m) in percentage of the chord (airfoil length), the second indicates the position of the maximum camber (p) in tenths of chord, and the last two numbers provide the maximum thickness (t) of the airfoil in percentage of chord. For example, the NACA 2415 airfoil has a maximum thickness of 15% with a camber of 2% located 40% back from the airfoil leading edge (or 0.4c). Utilizing these m, p, and t values, we can compute the coordinates for an entire airfoil using the following relationships:

- Pick values of x from 0 to the maximum chord c.
- Compute the mean camber line coordinates by plugging the values of m and p into the following equations for each of the x coordinates.

$$y_c = \frac{m}{p^2}(2px - x^2) \qquad where \quad 0 < x < p \qquad (3.1)$$

$$y_c = \frac{m}{1-p^2}([1 - 2p]) + 2px - x^2) \qquad where \quad p < x < C \qquad (3.2)$$

Where:

x = coordinates along the length of the airfoil, from 0 to c (which stands for chord, or

y = coordinates above and below the line extending along the length of the airfoil, these are either y_t for thickness coordinates or y_c for camber coordinates

t = maximum airfoil thickness in tenths of chord (i.e. a 15% thick airfoil would be 0.15)

m = maximum camber in tenths of the chord

p =position of the maximum camber along the chord in tenths of chord.

- Calculate the thickness distribution above (+) and below (-) the mean line by plugging the value of t into the following equation for each of the x coordinates.

$$\pm y_t = \frac{t}{0.2}\left(0.2969\sqrt{x} - 0.1260x - 0.3516x^2 + 0.2843x^3 - 0.1015x^4\right) \quad (3.3)$$

- Determine the final coordinates for the airfoil upper surface (X_U, Y_U) and lower surface (X_L, Y_L) using the following relationships.

$$X_U = x - y_t \sin\theta \quad (3.4)$$

$$Y_U = y_c + y_t \cos\theta \quad (3.5)$$

$$X_L = x + y_t \sin\theta \quad (3.6)$$

$$Y_L = y_c - y_t \cos\theta \quad (3.7)$$

Where $\theta = arctan\left(\frac{dy_c}{dx}\right)$

Therefore the airfoils final coordinates for upper and lower surface were found out with the help of above methodology for the fabrication of the airfoil body as shown in the table below:

X(along chord)	Y_U	Y_L
10	0	0
9.5	0.12	-0.066
8.8	0.27	-0.13
8.4	0.35	-0.17
7.9	0.44	-0.22
7.4	0.54	-0.27
6.8	0.63	-0.32
6.2	0.71	-0.37
5.6	0.79	-0.42
5	0.85	-0.46
4.5	0.90	-0.50
3.75	0.93	-0.53
3.14	0.95	-0.55
2.56	0.91	-0.56

1.53	0.80	-0.54
1.1	0.71	-0.51
0.73	0.60	-0.48
0.43	0.47	-0.42
0.21	0.34	-0.35
0	0	0

Table-3.1 Upper and Lower surface coordinates of airfoil body.

Specifications of the fabricated airfoil:

Chord	10 cm
Length	30 cm
Maximum chamber	0.2 cm
Position of maximum chamber on chord	4 cm
Maximum thickness	0.15 cm
Maximum thickness position	3.14 cm

Table-3.2 Main dimensions of the airfoil.

Figure 3.1 Fabricated airfoil body.

3.2 Experimental set-up

The set-up consists of an open circuit wind tunnel of length 6.25 m, inlet section (effuser) 900 mm × 900 mm, test section 950 mm × 300 mm × 300 mm, and outlet section (diffuser) 500 mm × 500 mm (Figure-8). The inlet section is connected to the test section by a smooth transition. The effuse accelerates fluid in the main stream from the rest and is provided with M.S. grid plates to prevent turbulence and to produce a uniform stream. The rectangular test section ensures two – dimensional flow. The test section is again connected to the diffuser by a smooth transition. The purpose of the diffuser is to convert the kinetic energy of the leaving fluid into pressure energy and to make the exit as efficient as possible. The driving unit of wind tunnel consists of an exhaust fan. The exhaust fan is fitted in the diffuse section. The wind speed is regulated by means of a rheostat (voltage regulator).

Figure 3.2 Wind tunnel set up at fluid mechanics lab (Thapar University).

A wooden airfoil of chord 100 mm and length of 300 mm equal to the width of test section is placed in the test-section such that axis of the airfoil is perpendicular to the direction of the flow. Pressure tapping (4 nos.), made of copper pipes are provided at front of leading edge and at the end of trailing edge and the left two are on the suction and pressure surfaces at the maximum thickness (15 mm) of airfoil. For easy location of pressure points, tags are fixed to each pressure tapping with the respective pressure

tapping number writing on it. For the measurement of static pressure of free stream, a hole is provided at the bottom of the test-section upstream of the airfoil. Inclined U-tube differential manometer containing water as the manometric liquid is used to measure the pressure difference. Prandtl-Pitot tube is used to measure the velocity of the flow in the test-section by connecting it to another inclined U-tube differential manometer containing water as the manometric liquid. A belt arrangement is provided on the top of the test-section to move the Pitot tube in the longitudinal direction. The airfoil is fixed in such a manner that the pressure tapping at $\theta = 0^0$ is the forward stagnation point which also gives the total head of free stream.

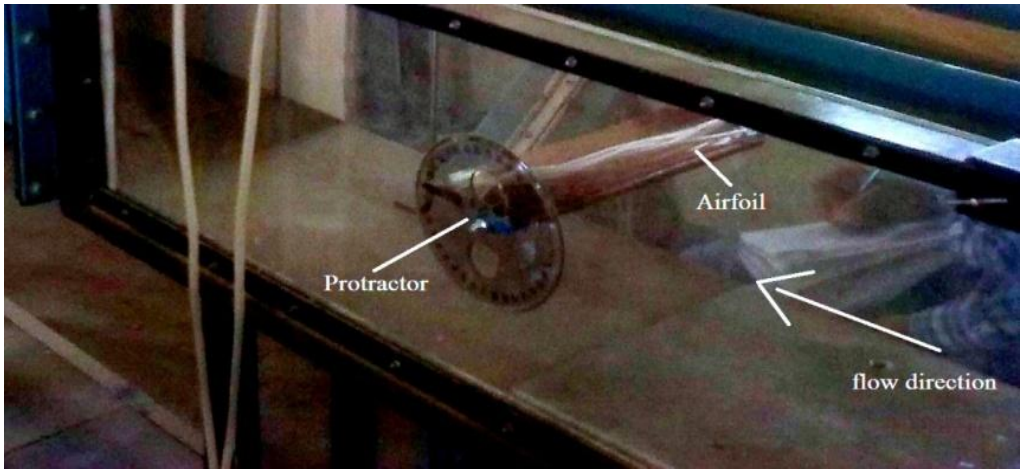

Figure 3.3 close view of test section with airfoil.

3.3 Procedure

- Start the exhaust fan by adjusting the speed with the help of rheostat.
- Connect static head tube to one limb of the inclined manometer. The other limb of the manometer is connected to pressure tapping No. 1 ($\theta=0^0$), keeping all other pressure tapping's closed.
- Note the difference in levels of the two limbs of the manometer-1, i.e. Δh.
- Repeat the above procedure for other pressure tapping's one by one, keeping the position of static head tube unchanged.
- Measure the velocity distribution along a vertical at upstream of the airfoil by connecting Prandtl-Pitot tube to another inclined U-tube manometer and again note the difference of the two limbs of the manometer-2 (i.e. Δx), for various vertical

positions of the Prandtl-Pitot tube. Take observation until the velocity becomes constant.

- Repeat all above steps for different Angle of Attacks (i.e. AoA -5^0 to 18^0).

3.4 Observations

Chord of the airfoil, C = 100 mm.

Specific weight of manometer liquid, γ_m = 9.757 kN/m^3

Specific weight of air, γ_a = 11.43 N/m^3

Density of air, ρ_a = 1.165 Kg/m^3

Inclination of manometer 1, θ_1 = 15^0

Inclination of manometer 1, θ_2 = 15^0

Formulae to be used

Differential pressure, $\Delta p = \Delta h(\gamma_m - \gamma_a) \sin \theta_1$ (3.8)

Local velocity, $u = \sqrt{2g\Delta x \sin\theta \left(\frac{\gamma_m}{\gamma_a} - 1\right)}$ (3.9)

3.5 Pressure Co-efficient

At any point in the flow where the local pressure is P the pressure coefficient C_P is defined as:

$$C_p = \frac{P - P_\infty}{\frac{1}{2}\rho U_\infty^2} \quad (3.10)$$

The total or stagnation Upstream Pressure P_T as measured by an impact probe (e.g. a pitot tube) is the sum of the static and dynamic pressure at that point, i.e.

$$P_T = P_\infty + \frac{1}{2}\rho U_\infty^2 \quad (3.11)$$

Thus, C_P may also written in terms of differential pressures:

$$C_P = \frac{P - P_\infty}{P_T - P_\infty} \quad (3.12)$$

The presence of the airfoil in the test section will affect the test section velocity. For example, at a 15^0 angle of attack the local velocity over the airfoil will increase to about

1.02 times the upstream velocity due to blockage of test section by the airfoil. This blocking effect will not be taken into consideration in the analysis that follows.

3.6 Lift and Pressure Drag

3.6.1 Normal Pressure Force

In the figure 11 below, the normal pressure force Pds, acting on a small region, may be resolved into components dX and dZ acting parallel and perpendicular to the chord, respectively.

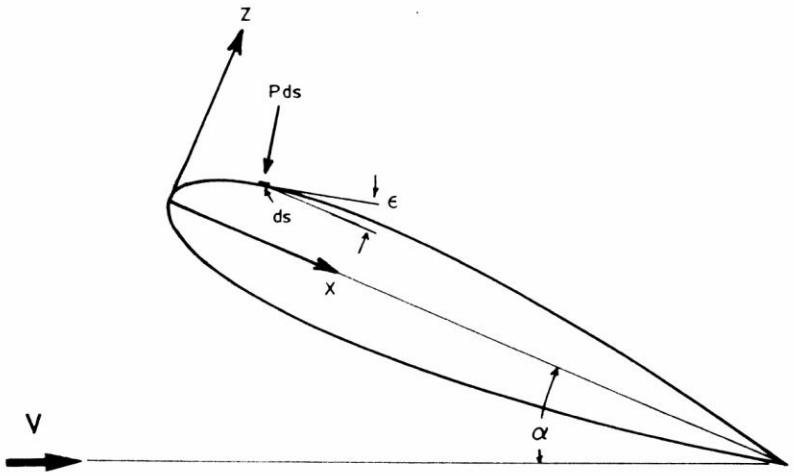

Figure 3.4 Normal pressure force on an airfoil surface.

On the upper surface the z component is given by:

$$dZ = -(P- P_{\infty})_U \, ds \cos \varepsilon \qquad (3.13)$$

The normal force Z per unit span and chord is given by:

$$dZ = - (P- P_{\infty})_U \, dx \qquad (3.14)$$

where $dx = ds \cos \varepsilon$. Similarly, Z on the lower surface is given by:

$$dZ = (P- P_{\infty})_L \, dx \qquad (3.15)$$

Therefore, the total force in the z direction may be written as:

$$Z = \int_0^c [\,(P - P_\infty)_U - (P - P_\infty)_L\,]dx \qquad (3.16)$$

The normal force coefficient then becomes:

$$C_z = \frac{Z}{\frac{1}{2}\rho U_\infty^2 c} \qquad (3.17)$$

3.6.2 Pressure Drag

The force coefficient parallel to the chord is responsible for pressure drag on airfoil, and this coefficient may be derived in a manner similar to that previously employed for the normal pressure force.

First, divide the airfoil into 2 sections, fore and aft, such that fore is the area in front of the maximum thickness point of the airfoil as indicated in figure 12:

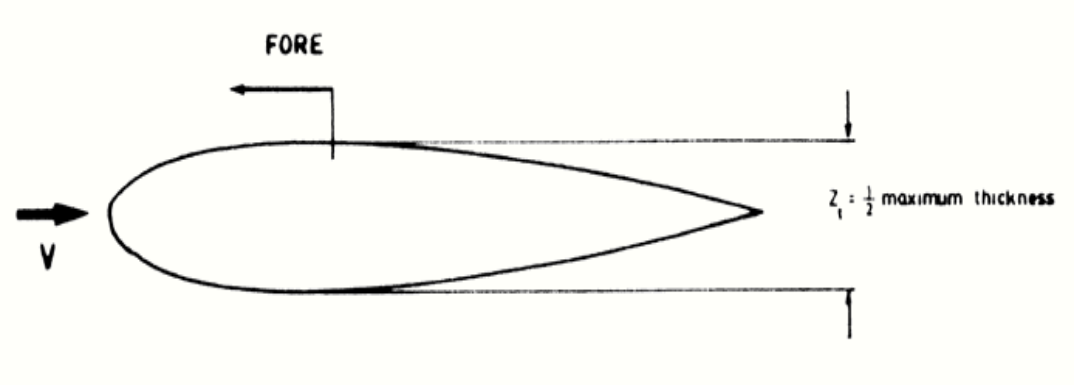

Figure 3.5 Pressure regions on an airfoil

For the fore section of the airfoil the x-component is given by:

$$dX = -(P - P_\infty)_U \, ds \sin \varepsilon \qquad (3.18)$$

The force per unit span acting along the chord line is then given by:

$$dX = (P - P_\infty)_F \, dz \qquad (3.19)$$

Where $dz = ds \sin \varepsilon$

Similarly for the aft section the x-component is given by:

$$dX = -(P - P_\infty)_A \, dz \tag{3.20}$$

Therefore the total force per unit span in the x-direction can be written as:

$$X = \int_{-z_t}^{z_t} (P - P_\infty)_F \, dz - \int_{-z_t}^{z_t} (P - P_\infty)_A \, dz \tag{3.21}$$

The corresponding force coefficient is then given by:

$$C_z = \frac{X}{\frac{1}{2}\rho U_\infty^2 c} \tag{3.22}$$

3.7 Lift and Drag Coefficients

Once the values of C_Z and C_X have been computed they may be used to calculate the lift and the drag coefficients C_L and C_D using the following force relationships.

$$C_L = C_Z \cos\alpha - C_X \sin\alpha \tag{3.23}$$

$$C_D = C_Z \sin\alpha + C_X \cos\alpha \tag{3.24}$$

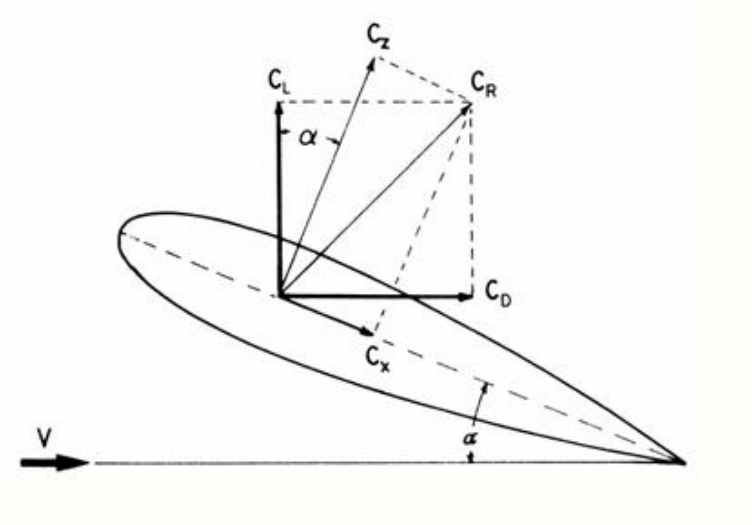

Figure 3.6 Component of airfoil

3.8 Results

3.8.1 Velocity Distribution

Measurement of velocity distribution along a vertical at upstream of the airfoil by connecting Prandtl-Pitot tube to inclined U-tube manometer and by again noting the difference of the two limbs of the manometer-2 (i.e. Δx), for various vertical positions of the Prandtl-Pitot tube until the velocity becomes constant. The local velocity (u) is find out by using equation 3.9 above and various values of velocity are shown in table 3 as shown below:

Sr. No.	Y(Vertical Positions) in mm	u (Velocity) in m/s
1	2	9.86
2	4	11.26
3	6	12.34
4	8	12.98
5	10	13
6	12	13.17
7	14	14.02
8	16	14.53
9	18	14.83
10	20	14.83
11	25	14.83
12	30	14.97
13	35	14.97
14	40	14.97
15	45	14.97

Table 3.3 shows the values of velocity distribution along vertical position of Prandtl-Pitot tube.

Therefore the Free Stream velocity, U_∞= 14.97 m/s.

After finding the free stream velocity, the value of Reynolds number and Mach number are calculated to check the flow behavior of the air in wind tunnel. Therefore the value of Reynolds number is 1.04×10^5 and the value of Mach number is 0.04.

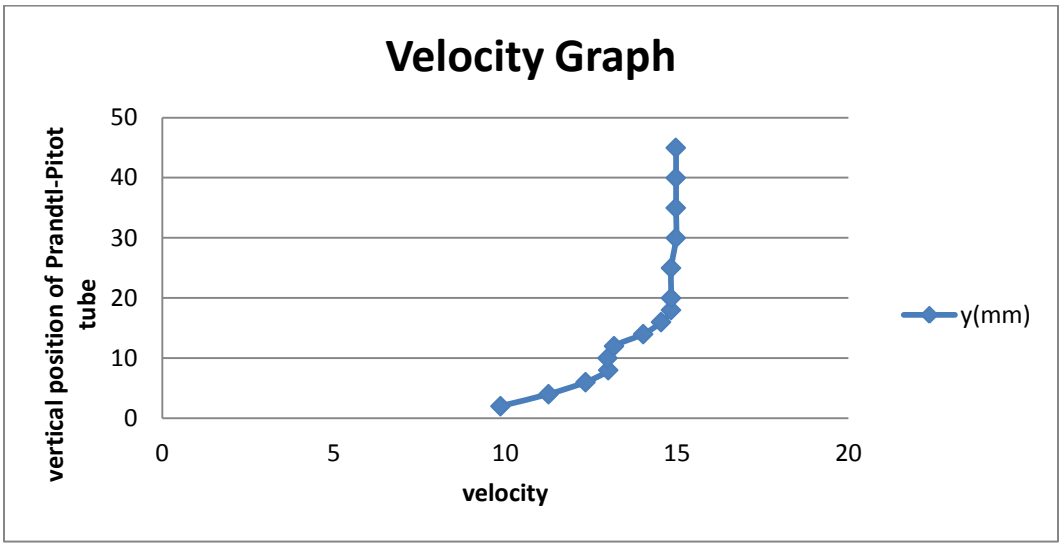

Figure 3.7 velocity distributions along vertical position of Prandtl-Pitot tube.

3.8.2 Lift and Drag

Lift and drag coefficients are calculated by using the equations 3.23 and 3.24 above the lift and drag forces are then carried out by multiplying the coefficients by $1/2\rho U^2$. The lift and drag (L/D) ratio is find out at different angle of attacks and 17^0 is the best angle found out which has the highest value of L/D along with angle of attack. The table 4 shows the values of lift and drag forces and coefficients values at various Angle of attacks (AoA) as below:

AoA	CL	CD	L(Lift force)	D(Drag force)	L/D
-5	-0.611	0.22	-2.51	0.90	-2.77
-2	-0.275	0.26	-1.13	1.06	-1.05
0	0.044	0.28	0.18	1.15	0.15
2	0.19	0.29	0.78	1.19	0.65
4	0.26	0.28	1.06	1.15	0.92
6	0.44	0.29	1.808	1.19	1.51
8	0.54	0.32	2.21	1.31	1.68

10	0.66	0.34	2.71	1.39	1.94
12	0.79	0.36	3.24	1.47	2.19
14	0.93	0.41	3.82	1.68	2.26
16	1.09	0.44	4.47	1.80	2.47
17	1.22	0.48	5.01	1.97	2.54
18	0.99	0.53	4.06	2.17	1.86

Table 3.4

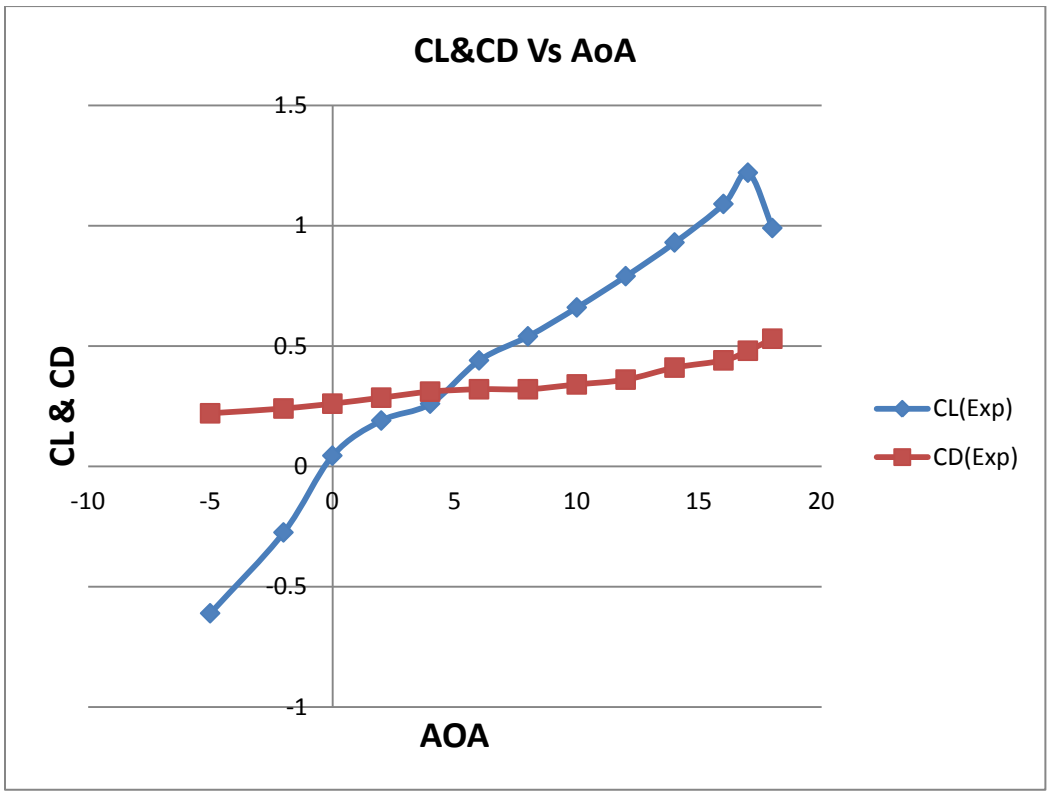

Figure 3.8 Coefficient of lift and drag vs angle of attack.

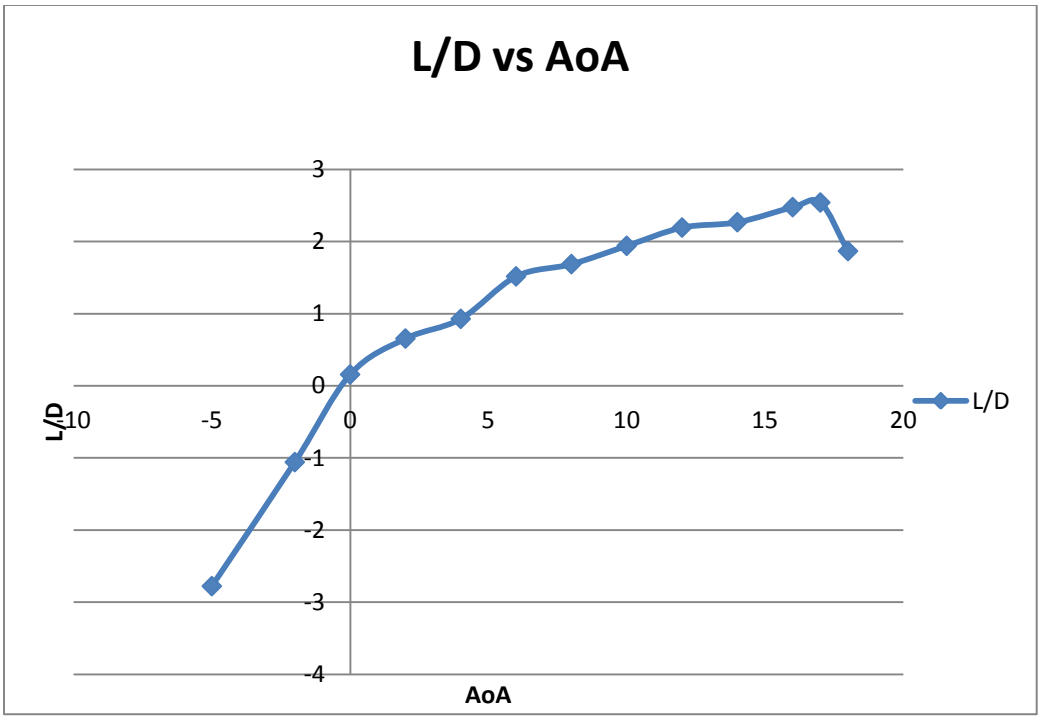

Figure 3.9 Lift to drag ratio (L/D) Vs Angle of attack (AoA)

CHAPTER-4

NUMERICAL EVALUATION OF AIRFOIL (CFD)

4.1 Background

CFD is a numerical method used to simulate physical problems with use of governing equations. This method can be used to investigate design approaches without creating a physical model – and can be a valuable tool to understand conceptual properties of new mechanical designs. By using a simulation instead of doing lab experiments, one may acquire results faster and with less expense.

An important aspect in the use of CFD is to understand the simplifications in software, and know the limitations in the computed results. Though the CFD software uses well known governing equations, severe simplifications are made in terms of grid and representing geometries.

4.2 Approach

Following is the method employed to carry through the CFD simulation:

4.2.1 Prepare geometric model.

4.2.2 Meshing

4.2.3 Boundaries.

4.2.4 Software (Fluent) set up, initialization and solving.

4.2.1 Preparing the model

NACA 2415 airfoil geometry was acquired as co-ordinate vertices i.e. texts file and imported into the Gambit software. Some minor adjustments were made to this to correct the geometry and make it valid as a CFD model.

Gambit is essential in the process of doing the CFD analysis: it creates the working environment where the object is simulated. An important part in this is creating the mesh surrounding the object. This needs to be extended in all directions to get the physical

properties of the surrounding fluid – in this case moving air. The mesh and edges must also be grouped in order to set the necessary boundary conditions effectively.

4.2.2 Meshing

An environment consisting of 2 squares and 1 semicircle surrounds the NACA 2415 airfoil. The mesh is constructed to be very fine at regions close to the airfoil and with high energy, and coarser farther away from the airfoil. For this airfoil a structured quadratic mesh was used.

Due to limitations in the FLUENT software, the mesh has to be fine also in certain regions far from the airfoil. A fine mesh implies a higher number of calculations which in turn makes the simulation use longer time to finish. For the NACA 2415 airfoil, the very front has an edge grid distributed with an increasing distance between nodes, starting from very small sizes. From the point of max thickness on the airfoil to the very back an even number of points is distributed on the airfoil surface.

Grid convergence: Four different meshes are made to the CFD simulations. This is to test the grid convergence – how the change in number of cells, and hence also cell size, affect the end result.

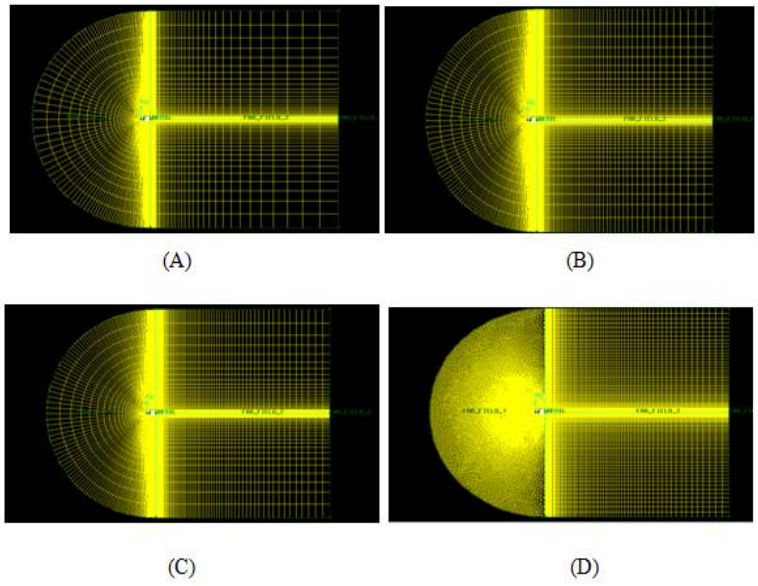

Figure 4.1 these illustrations show the four different mesh set ups for the CFD simulation

As per calculating the end results on the above different types of mesh ups and comparing these end results with the experimental data are shown in table 5 as below:

Grids(QUAD)	CL(AOA=10)	CL(experimental)	Deviation	Skewness
Figure 17(A) Mesh size-60×45 Elements-12,195	0.7358	0.66	-0.0758	0.22
Figure 17(B) Mesh size-80×65 Elements-16,200	0.629	0.66	0.031	0.18
Figure 17(C) Mesh size-90×70 Elements-19,000	0.625	0.66	0.035	0.19
Figure 17(D) Grids(TRI+QUAD) Mesh size-100×65 Elements-33,642	0.578	0.66	0.082	0.45

Table 4.1 Grid test

Lift coefficient is calculated at Angle of attack i.e. 10^0. Comparison of the end results of different mesh files and the experimental data shows the minimum deviation of results with the quadrilateral meshing having mesh size 90×70 and number of elements 16,200 as shown above in figure 17(B). After that mesh results are not so much affected by followed mesh ups so the all simulations are done on the same mesh file and validating the final results with experimental data.

4.2.3 Setting boundary conditions

Giving properties to the different geometries is vital to make the simulation work. In this case, the mesh boundaries were given set to the x and y velocity components, and the end

boundary the property “pressure-outlet” to simulate the zero gauge pressure. The airfoil itself is given as wall properties.

4.2.4 Setting up Fluent

The geometries and mesh were imported into FLUENT, and the system and environment properties set. “PRESTO!” and “Double precision” is selected as system parameters, ensuring adequate accuracy. FLUENT has single precision as default, but for these simulations an accurate solution is requested. The residuals for the different turbulence model variables were set to 10^{-8} and the iteration max count to 1000. The simulation process could also be halted or stopped if the CL or CD seemed to have stabilized properly.

4.2.4.1 Viscosity models

Considering vortex shedding and boundary layer separation for airfoils and wings, this simulation will have to deal with turbulent flows. The chaotic nature of turbulent flow makes it very expensive to compute velocities for all points in space. RANS is the opposite to DNS which is the analytic direct simulation of the governing equations, and use a statistical and averaged approach to find the flow behavior. The reason for using RANS models is that small vortices – in turn very expensive to solve - are removed by averaging the flow.

A crucial point is selecting a viscous model, and in FLUENT there are several options. There are fundamental differences to the different models, and may be used for different types of flows. In this, the viscous models k-ε and Spalart-Allmaras and k-ω are used. k-ε and k-ω are 2-equation models, whilst Spalart-Allmaras (S-A) is a newer 1-equation model.

4.3 Results and discussion

With knowledge of the wind tunnel experiment, the simulations of the NACA-2415 airfoil model were repeated for a number of angles of attack from -5 to 18 degrees.

4.3.1 Qualitative results

Viscous models k-ε, k-ω and Spalart-Allmaras are compared. And the different contour outputs from the simulations are as shown below:

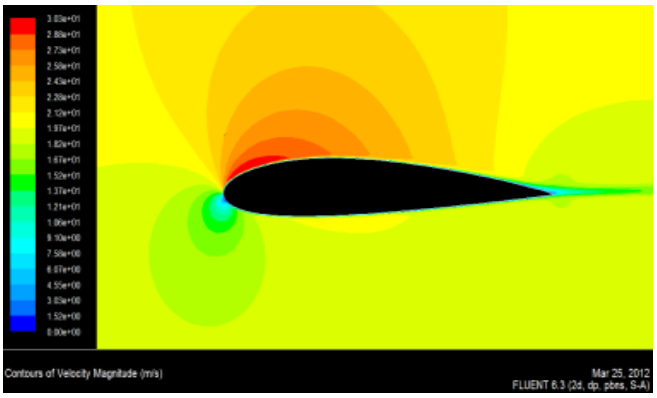

Figure 4.2 Velocity contours (-5^0 Angle of attack and viscosity model S-A).

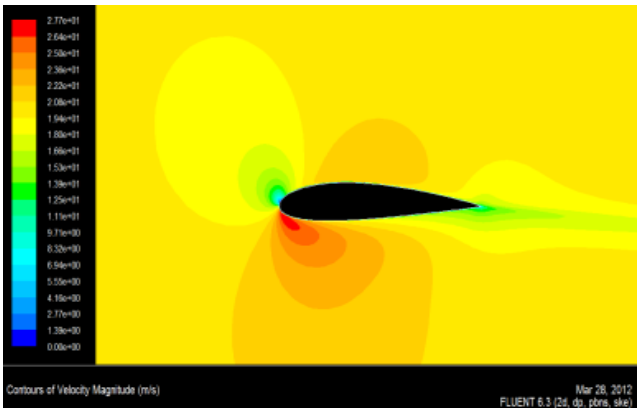

Figure 4.3 Velocity contour (-5^0 Angle of attack and viscosity model k-ε).

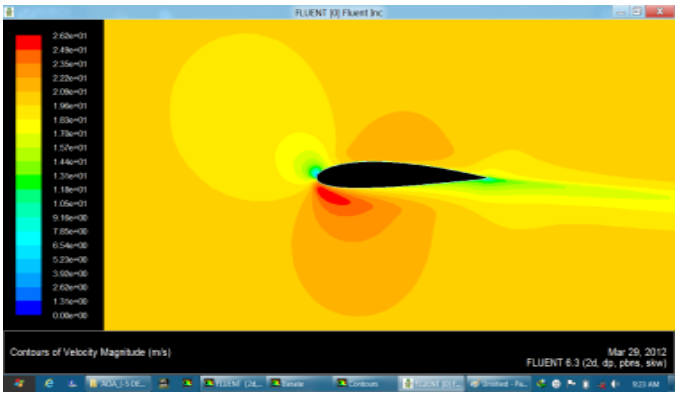

Figure 4.4 Velocity contour (-5^0 Angle of attack and viscosity model k-ω).

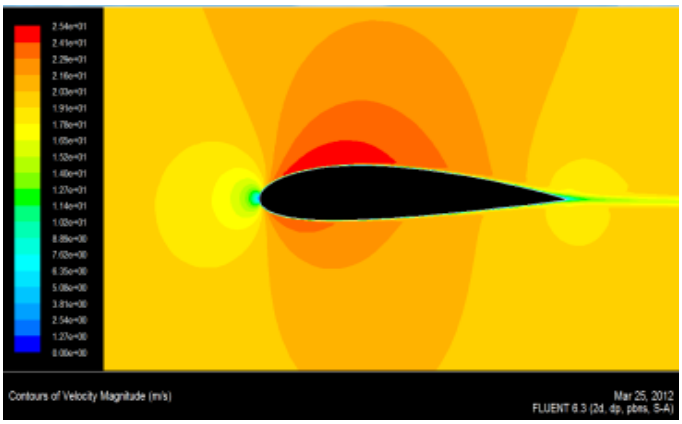

Figure 4.5 Velocity contour (0^0 Angle of attack and viscosity model S-A).

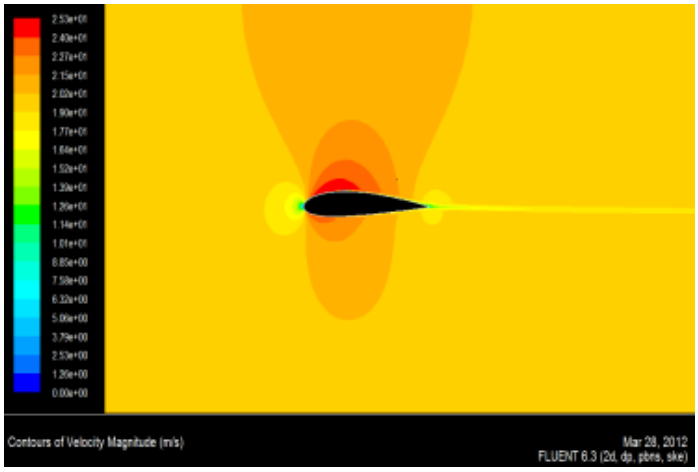

Figure 4.6 Velocity contour (0^0 Angle of attack and viscosity model k-ε).

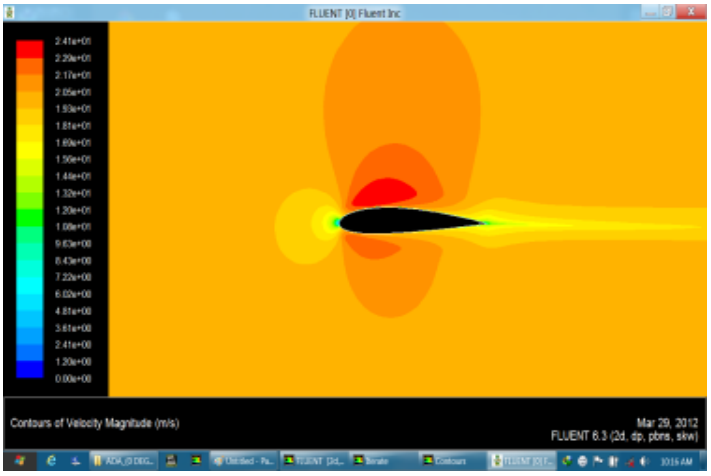

Figure 4.7 Velocity contour (0^0 Angle of attack and viscosity model k-ω).

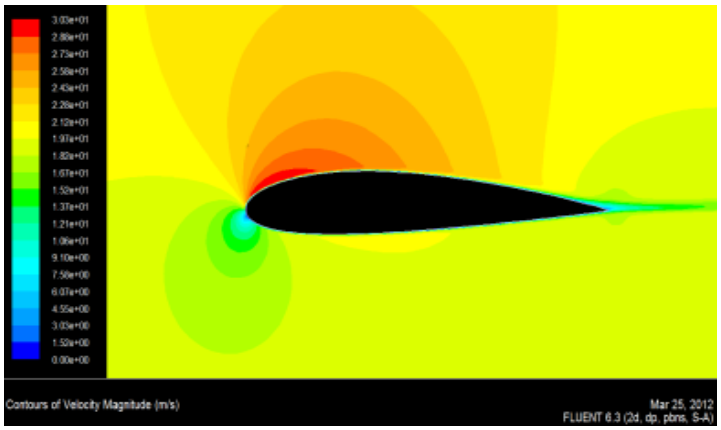

Figure 4.8 Velocity contour (5^0 Angle of attack and viscosity model S-A).

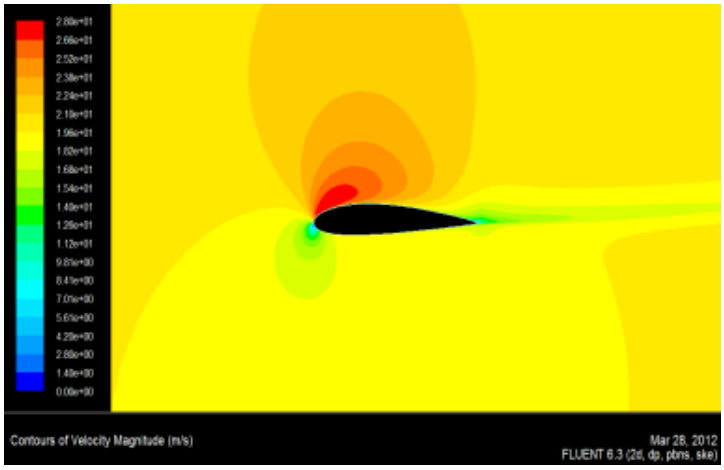

Figure 4.9 Velocity contour (5^0 Angle of attack and viscosity model k-ε).

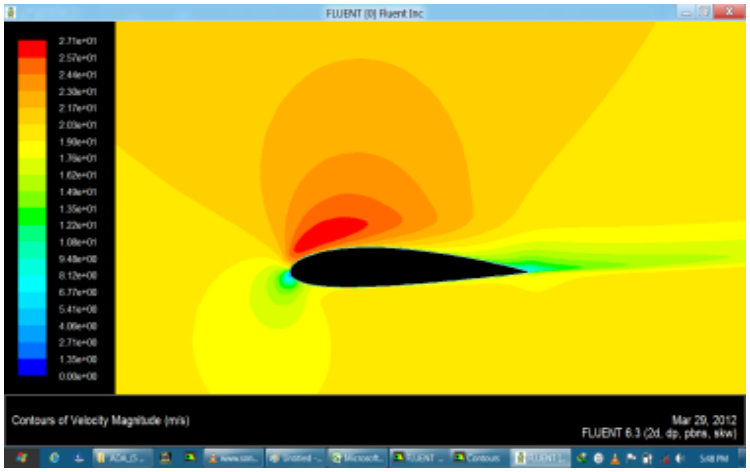

Figure 4.10 Velocity contour (5^0 Angle of attack and viscosity model k-ω).

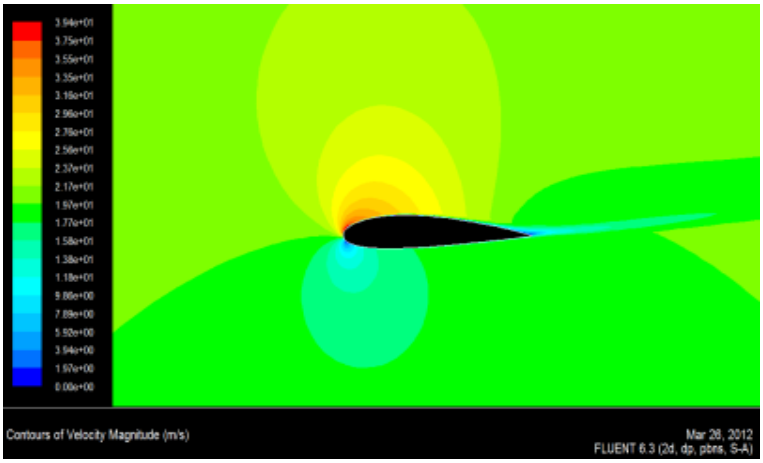

Figure 4.11 Velocity contour (10^0 Angle of attack and viscosity model S-A).

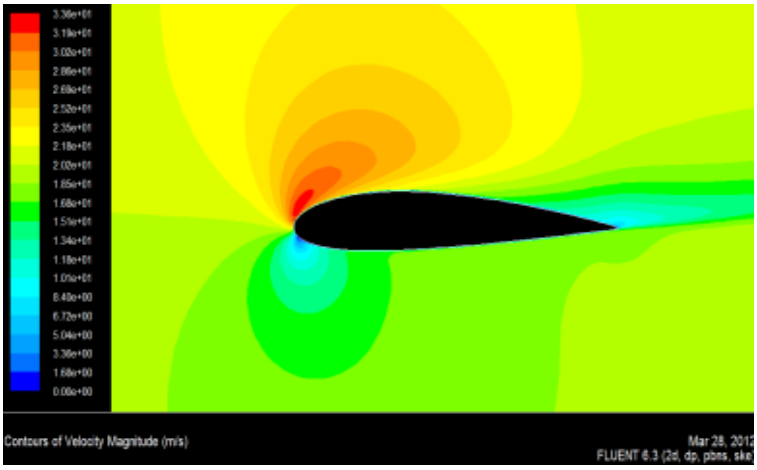

Figure 4.12 Velocity contour (10^0 Angle of attack and viscosity model k-ε).

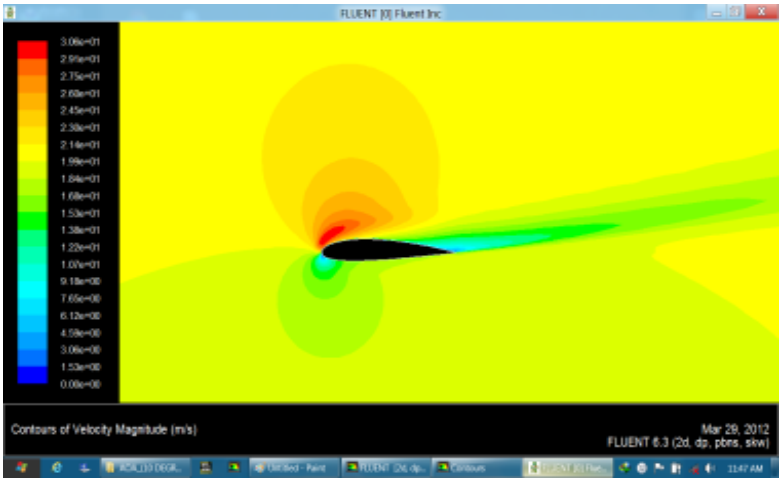

Figure 4.13 Velocity contour (10^0 Angle of attack and viscosity model k-ω).

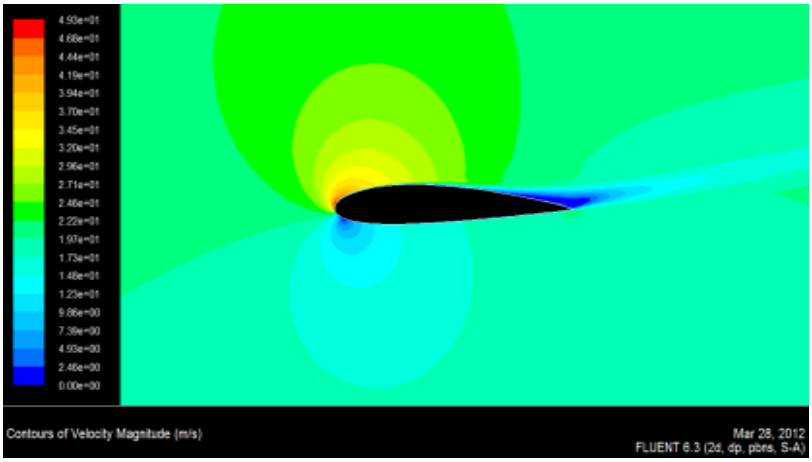

Figure 4.14 Velocity contour (15^0 Angle of attack and viscosity model S-A).

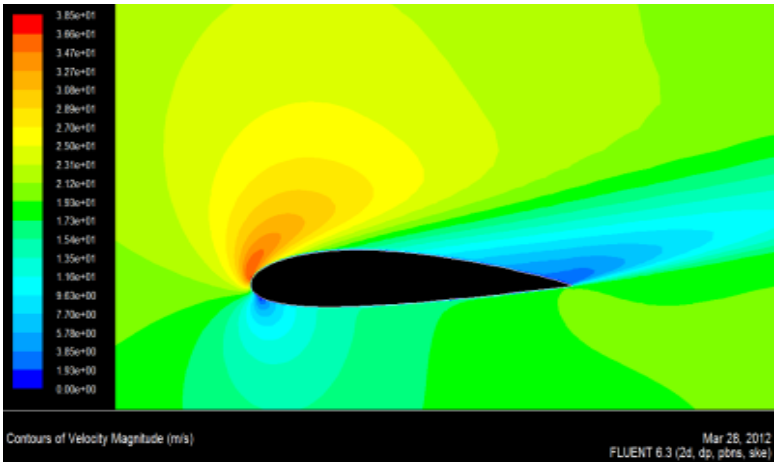

Figure 4.15 Velocity contour (15^0 Angle of attack and viscosity model k-ε).

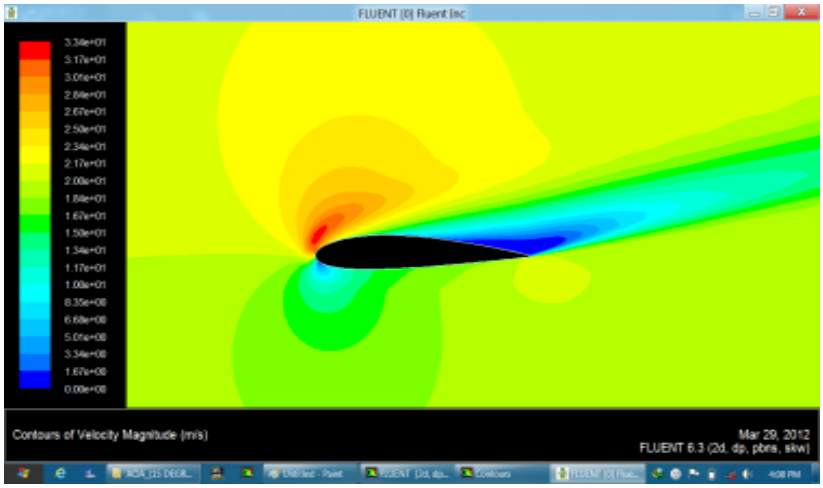

Figure 4.16 Velocity contour (15^0 Angle of attack and viscosity model k-ω).

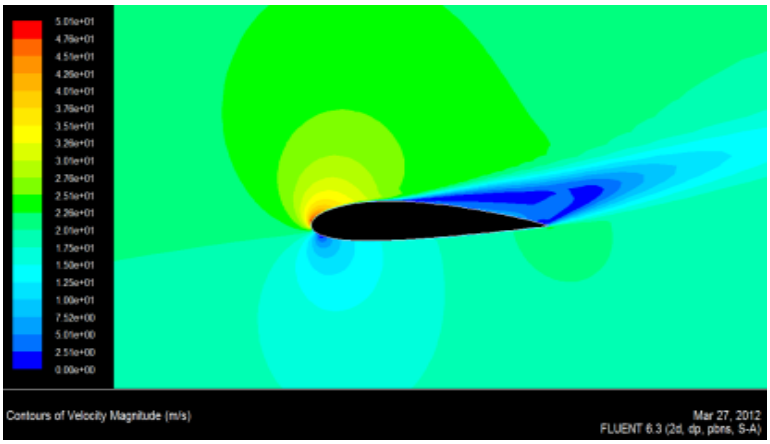

Figure 4.17 Velocity contour (18^0 Angle of attack and viscosity model S-A).

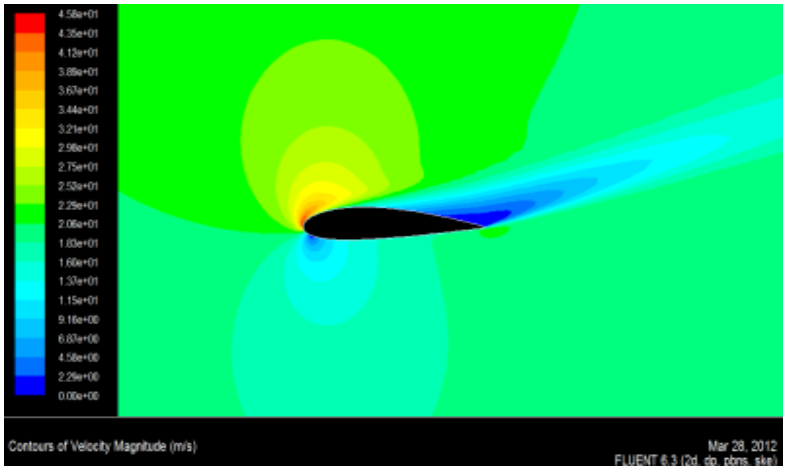

Figure 4.18 Velocity contour (18^0 Angle of attack and viscosity model k-ε).

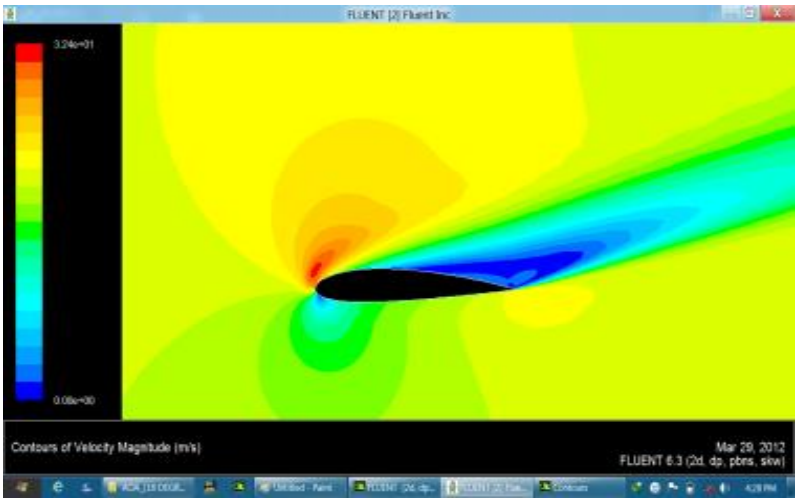

Figure 4.19 Velocity contour (18^0 Angle of attack and viscosity model k-ω).

4.3.2 Performance coefficients

Comparing the results from the CFD simulation and the experimental wind tunnel data for the NACA 2415 airfoil, yields a good correlation for lift slope and stall angle.

(A) Lift coefficient

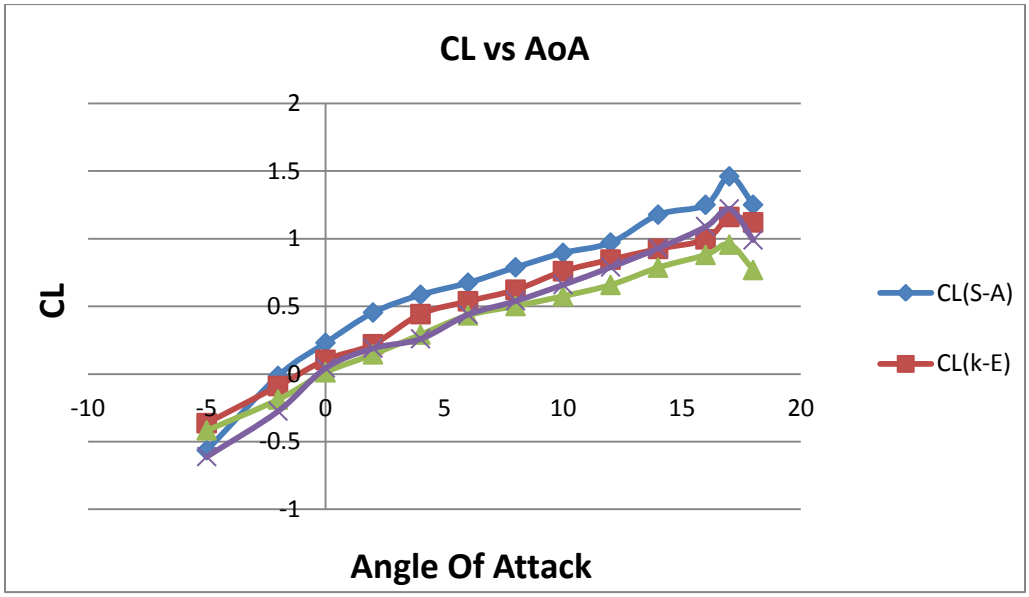

Figure 4.20 Coefficient of lift Vs Angle of Attack.

(B) Drag coefficient

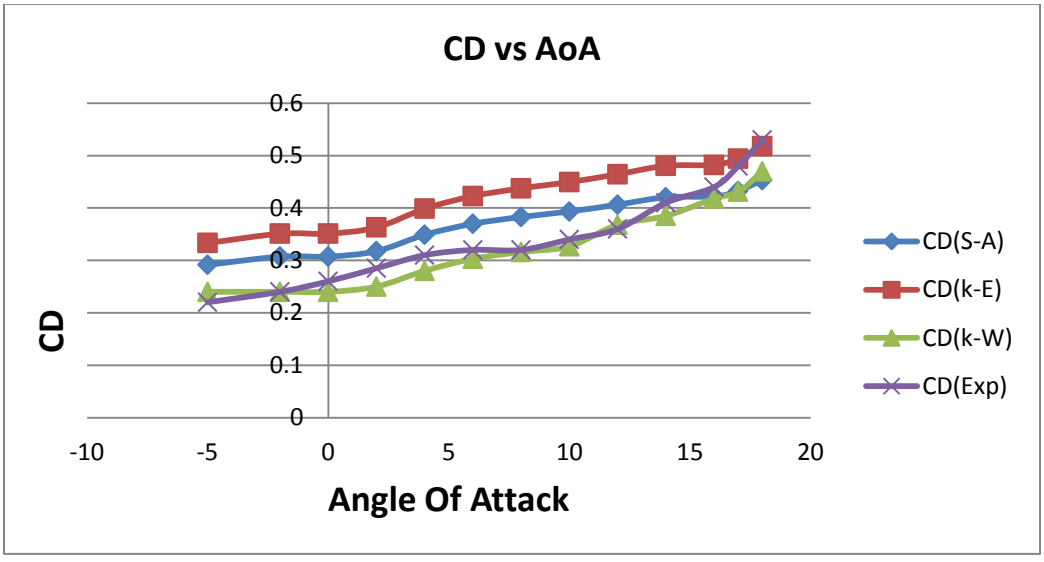

Figure 4.21 Coefficient of drag Vs Angle of Attack.

(C) Lift and drag coefficients Vs Angle of attack

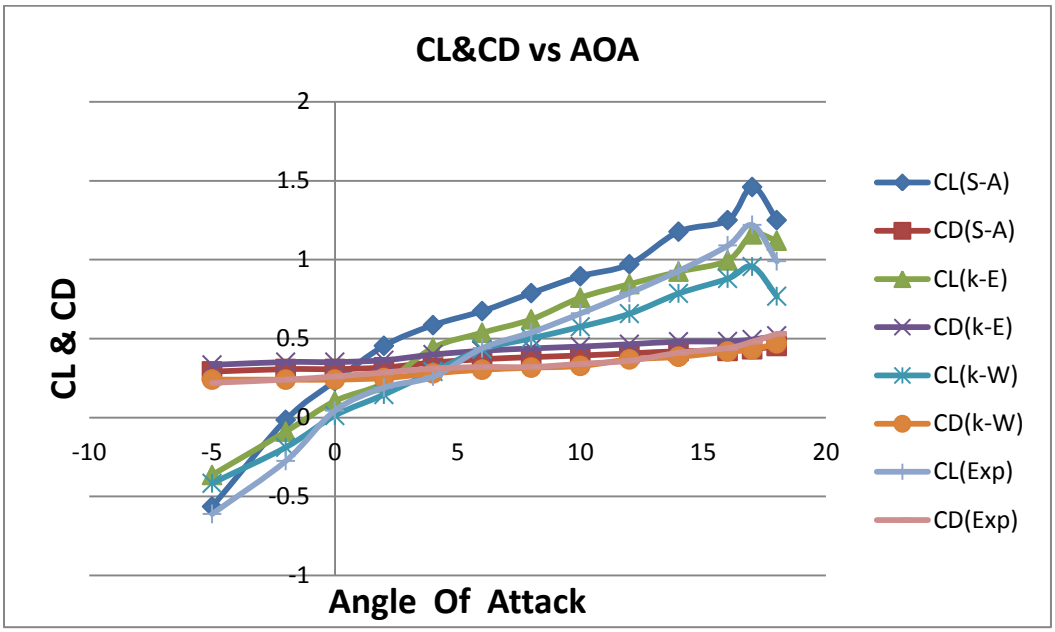

Figure 4.22 Coefficient of lift and drag Vs Angle of Attack.

(D) Lift to Drag force

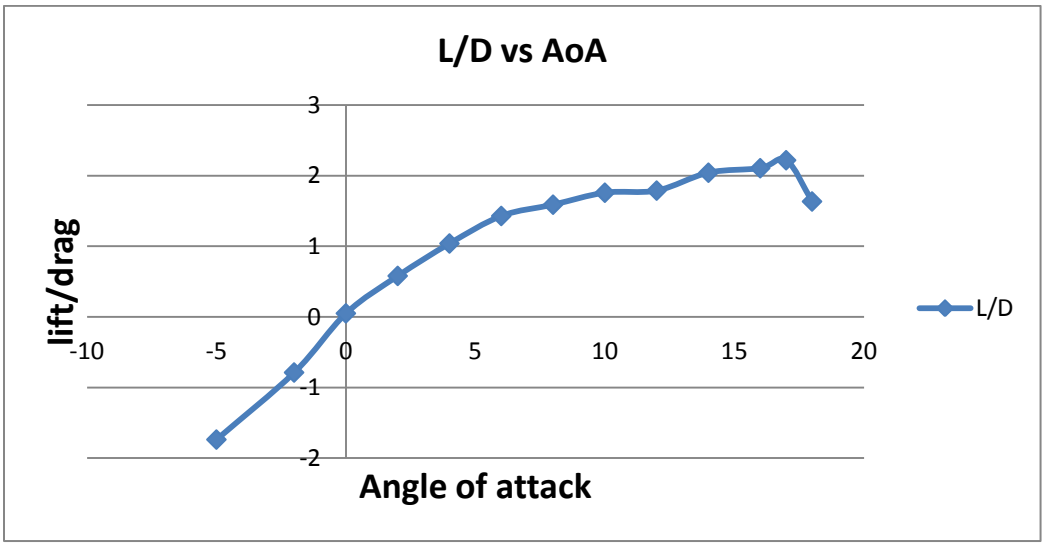

Figure 4.23 Lift/Drag ratios Vs Angle of Attack.

Comparing the graphs, a clear correlation can be found between the experimental data and the simulations. All the turbulent models follow the slope of the experimental data. The k-ω model gives the most nearer results to the experimental and identifies the stall angle at 17°.

For CD only k-ω shows satisfactory correlation to the experimental data. Considering the quite similar performance in determining CL, k-ω seems like the overall best turbulence model to use.

4.3.3 Pressure distribution

The pressure distributions on the airfoil surface are shown in Figures 4.6.1, 4.6.2 and 4.6.3 at three attack angles α= 0^0, 6^0 and 15^0, where $C_p = \frac{P-P_\infty}{\frac{1}{2}\rho U_\infty^2}$ is the pressure coefficient.

For the validation of the CFD results the data is compared with reference [9] and the pressure distribution is shown in figures as below:

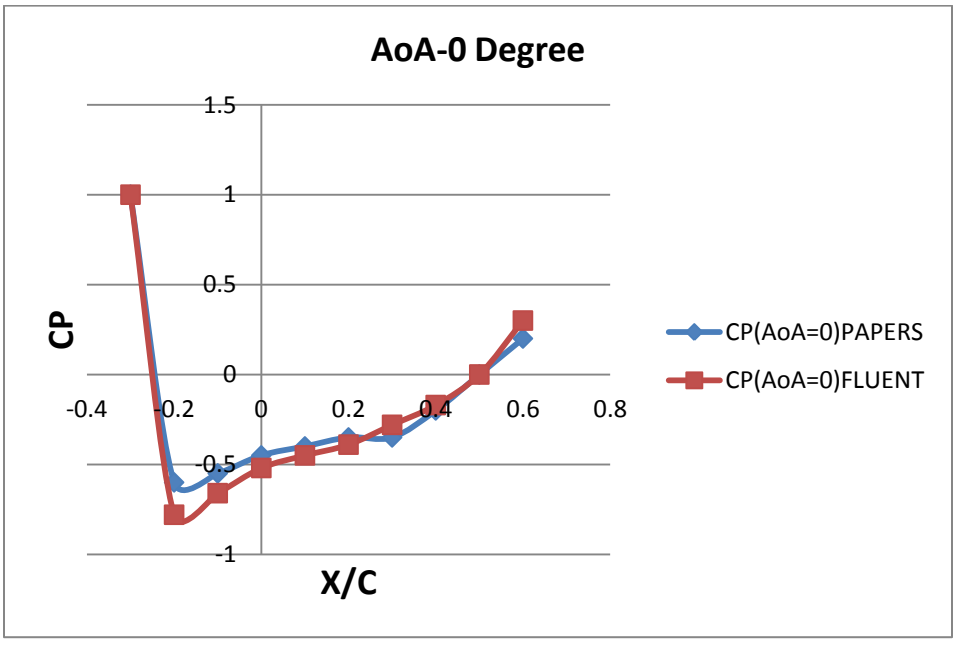

Figure 4.24 Pressure coefficients Vs X/C at Angle of Attack 0^0.

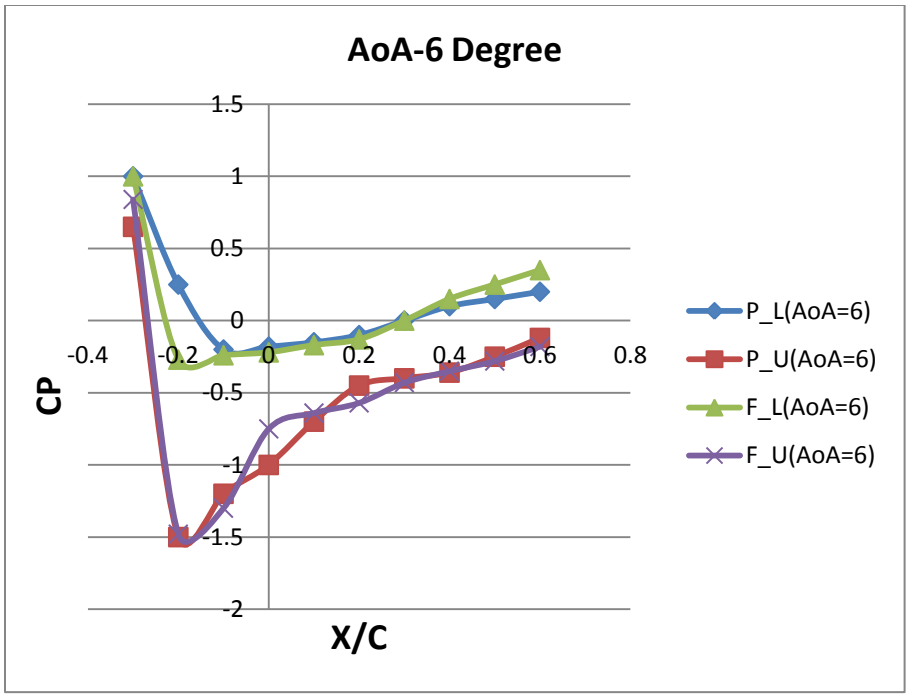

Figure 4.25 Pressure coefficients Vs X/C at Angle of Attack 6^0.

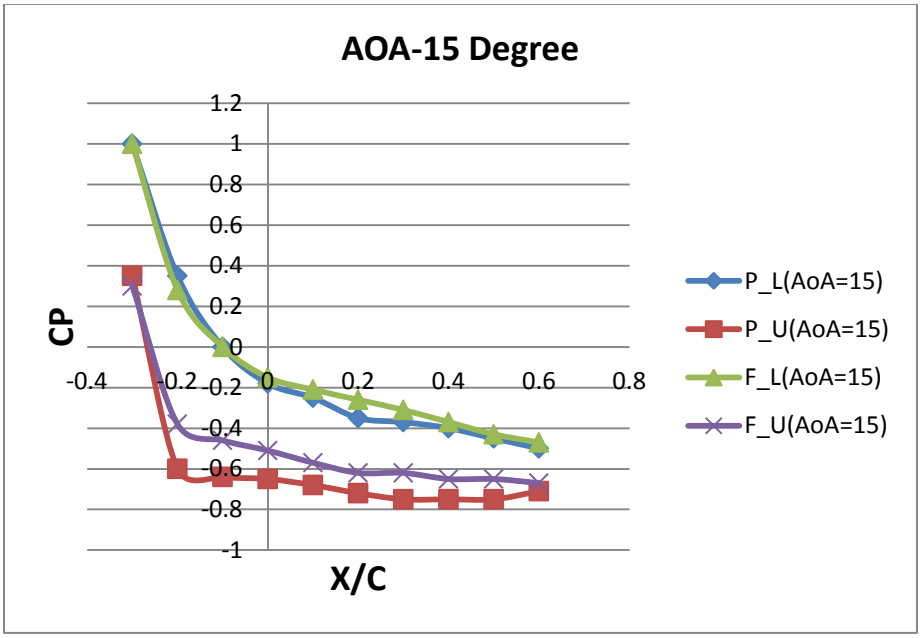

Figure 4.26 Pressure coefficients Vs X/C at Angle of Attack 15^0.

The result indicates that the pressure coefficient increases gradually along the airfoil surface except for the region near the leading edge. With an increase in attack angle to $\alpha = 6^0$, the pressure distribution becomes asymmetrical about the airfoil axis. The pressure on

the suction surface shows a large negative value just downstream of the leading edge of the airfoil, while the pressure on the pressure surface indicates a positive value except for the middle region along the chord.

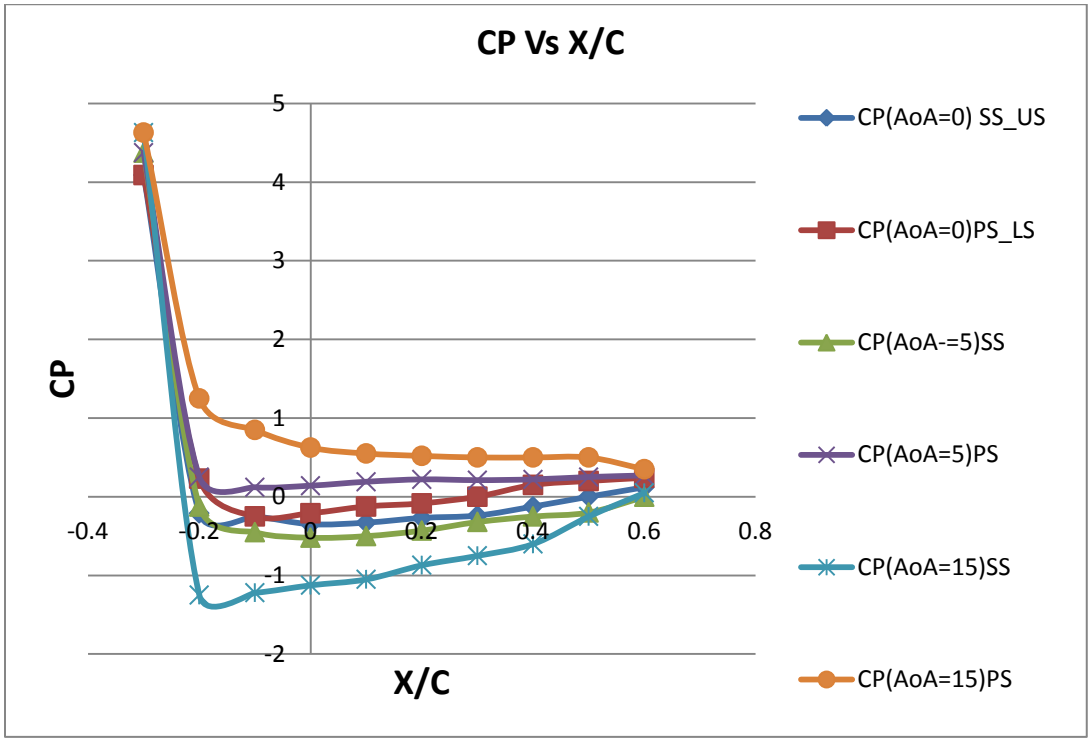

Figure 4.27 Pressure coefficient Vs X/C at Angle of Attack $\alpha = 0^0$, 6^0 and 15^0. For_NACA_2415

Thus, the pressure level on both sides of the airfoil increases gradually along the airfoil surface to form adverse pressure gradients on the airfoil surfaces, which leads to the flow separation on the airfoil surfaces.

With further increase in attack angle to $\alpha = 15^0$,the pressure level on the suction surface increases near the leading edge and decreases in the rear region of the airfoil, which results in a uniform pressure distribution on the whole suction surface except for the near stagnation region. This suggests the formation of large separating region on the whole suction surface. The pressure distribution on the pressure surface experiences a gradual decrease along the airfoil surface and a formation of favorable pressure gradient, which suggest the presence of attached flow on the pressure surface.

4.3.4 Surface-flow visualization on airfoil surface

Figure 4.7 shows the separation and reattachment points on the airfoil at various angles of attack α, which are obtained from the Pressure contours by visualizing the value of pressure gradient i.e. dp/dx. The separation point occurs at the point where the value of pressure gradient goes positive to negative and the reattachment point occurs where it goes negative to positive value. The separation and reattachment points are identified by the stream wise distance x/C from the airfoil axis.

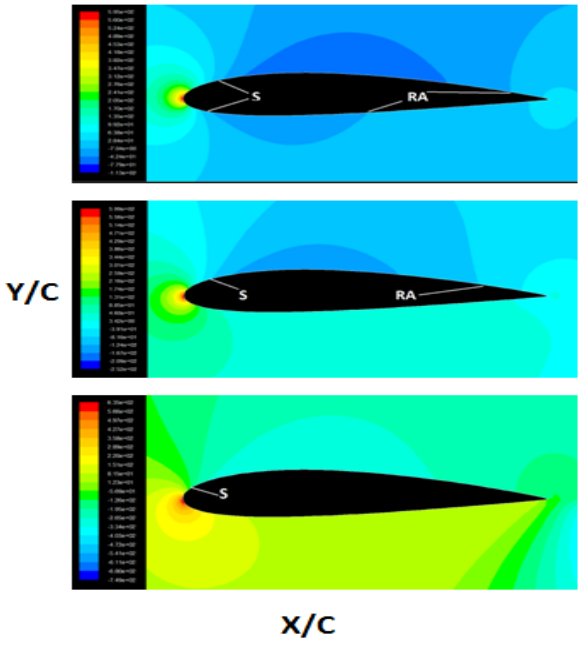

Figure 4.28 Separation and reattachment points are shown on the airfoil surface at attack angles, $\alpha=0^0$, 6^0 and 15^0 respectively.

With an increase in attack angle, the separation point on the suction surface moves to the leading edge of the airfoil and that on the pressure surface shifts to the trailing edge. The reattachment point is located downstream of the separation points on both sides of the airfoil. It is to be noted that the reattachment points disappear on the suction surface at an attack angle larger than 15^0, indicating the formation of a large separating region on the suction surface of the airfoil. While the flow under the pressure surface remain attached on the airfoils surface due to the presence of favorable pressure gradient.

CHAPTER-5

PROTOTYPING

5.1 Introduction

A prototype is an early sample or model built to test a concept or process or to act as a thing to be replicated or learned from. It is a term used in a variety of contexts, including design, electronics, and software programming. A prototype is designed to test and trial a new design to enhance precision by system analysts and users. Prototyping serves to provide specifications for a real, working system rather than a theoretical one.

Prototypes are the best way to convert your industrial ideas into tangible reality. Using CAD drawing techniques a specialist can produce a drawing of your yet to be realised final industrial product. With the help of computer simulations, the experts then convert the drawing into a prototype.

Prototyping of the airfoil body is done to check how much variations occurs in the results by comparing them with the experimental data as evaluated..

5.2 Preparing the geometric model

Modeling of NACA 2415 airfoil is done by scaling it to the actual size of the wing. Text file containing co ordinate vertices of the airfoil is imported into the gambit software. Some minor adjustments were made to this to correct the geometry and make it valid as a CFD model. Gambit is essential in the process of doing the CFD analysis: it creates the working environment where the object is simulated.

Specifications of the prototype (NACA 2415) airfoil:

Chord	100 cm
Length	800 cm
Maximum chamber	20 cm
Position of maximum chamber on chord	40 cm

Maximum thickness	15 cm
Maximum thickness position	31.4 cm

Table 5.1 specifications

5.3 Meshing

Meshing consists of the two rectangular and one semi circular regions around the airfoil for analyzing the flow behavior around the airfoil. The mesh is constructed to be very fine at regions close to the airfoil and with high energy, and coarser farther away from the airfoil. For this airfoil a structured quadratic mesh was used. Due to limitations in the FLUENT software, the mesh has to be fine also in certain regions far from the airfoil.

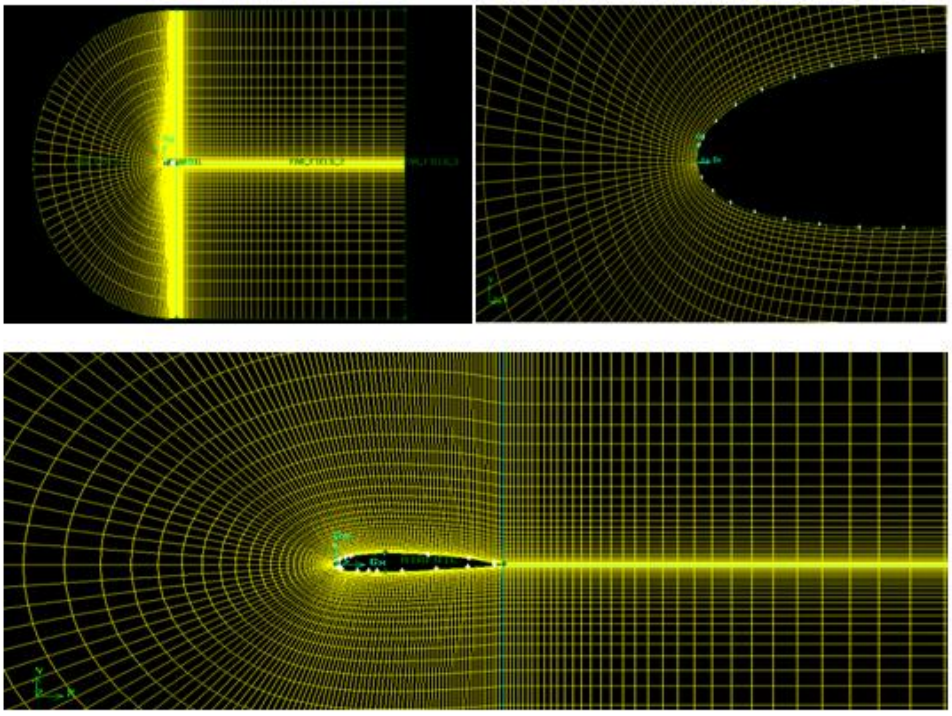

Figure 5.1 Meshing of the Prototype (NACA 2415)

Grids	Elements	Mesh size	Skewness
Quadrilateral mesh	23,400	60×45	0.64

Table 5.2 Parameter used in mesh

5.4 Setting up Fluent

The geometries and mesh were imported into FLUENT, and the system and environment properties set. "PRESTO!" and "Double precision" is selected as system parameters, ensuring adequate accuracy. FLUENT has single precision as default, but for these simulations an accurate solution is requested. The residuals for the different turbulence model variables were set to 10-8 and the iteration max count to 1000. The simulation process could also be halted or stopped if the CL or CD seemed to have stabilized properly.

5.5 Results

5.5.1. Different contour outputs of simulation

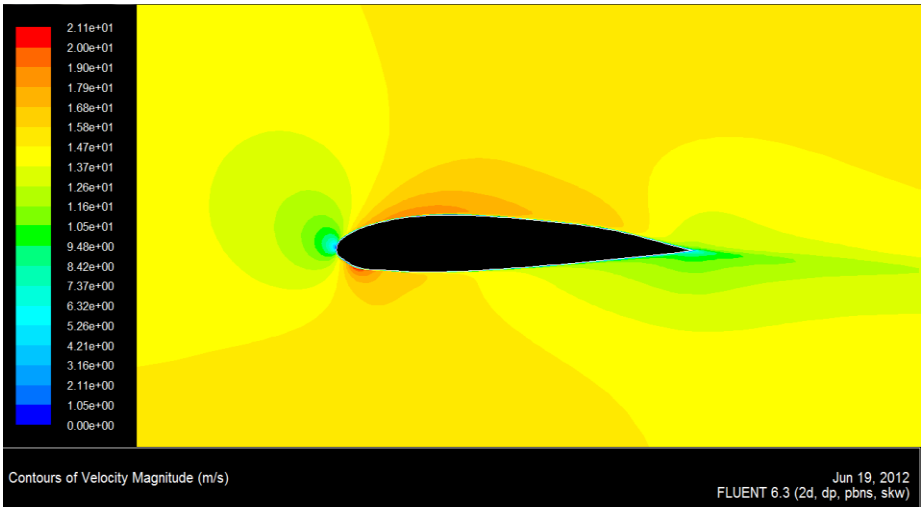

Figure 5.2 Pressure contour (-5^0 Angle of attack and viscosity model k-ω)

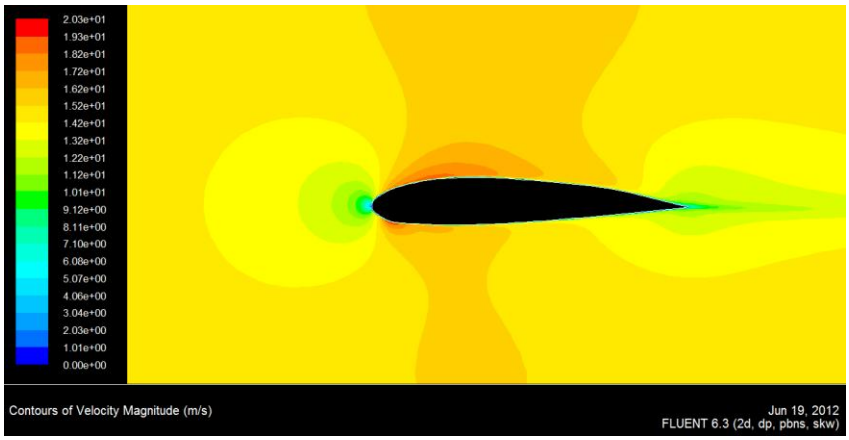

Figure 5.3 Pressure contour (0^0 Angle of attack and viscosity model k-ω)

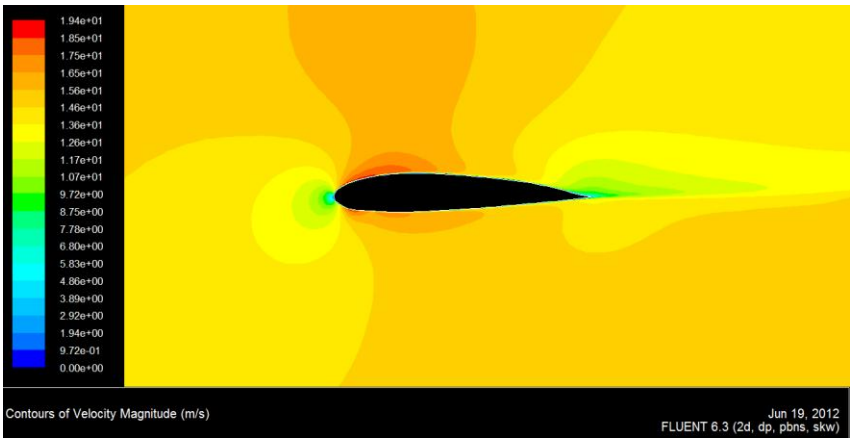

Figure 5.4 Pressure contour (5^0 Angle of attack and viscosity model k-ω)

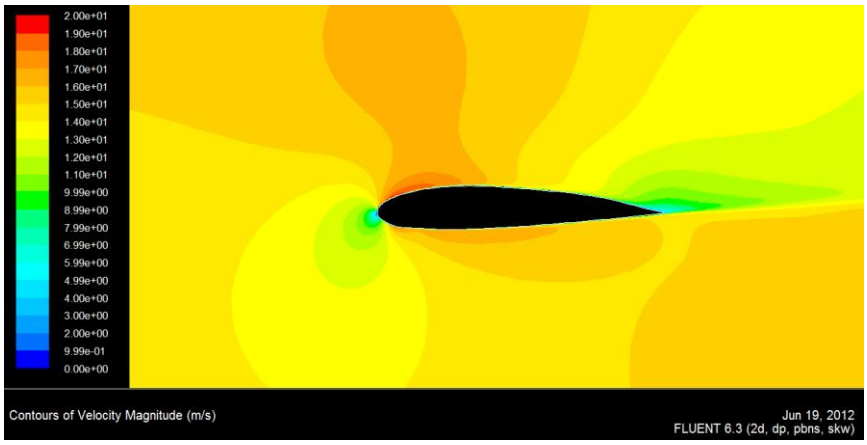

Figure 5.5 Pressure contour (10^0 Angle of attack and viscosity model k-ω)

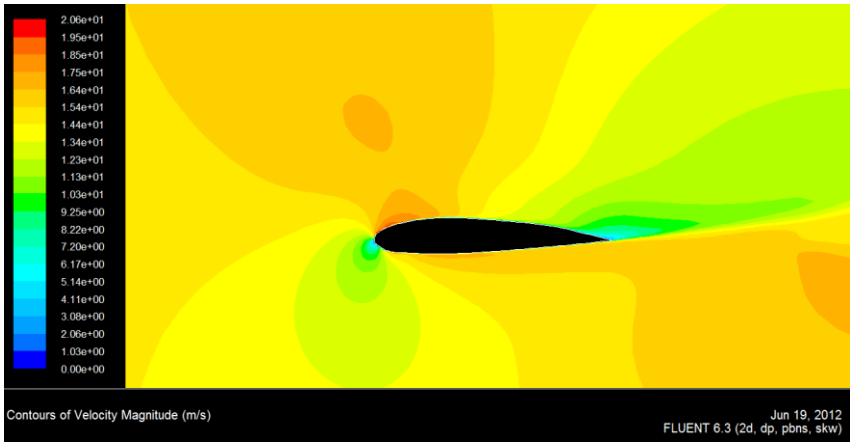

Figure 5.6 Pressure contour (15^0 Angle of attack and viscosity model k-ω)

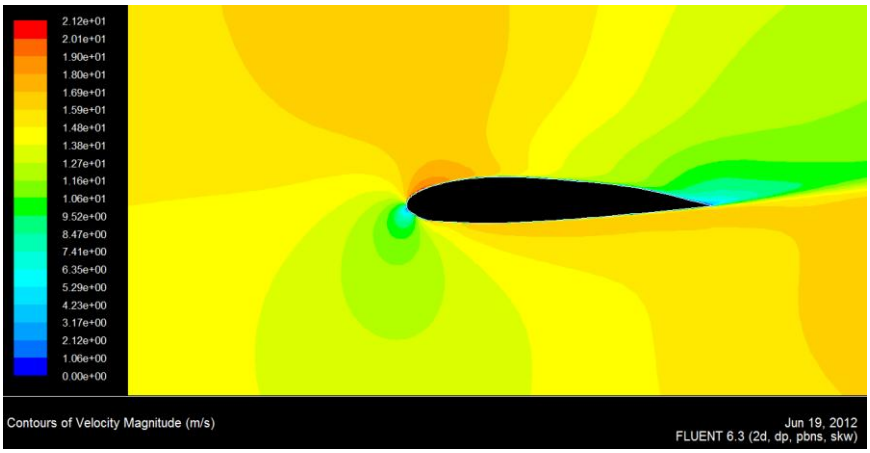

Figure 5.7 Pressure contour (17^0 Angle of attack and viscosity model k-ω)

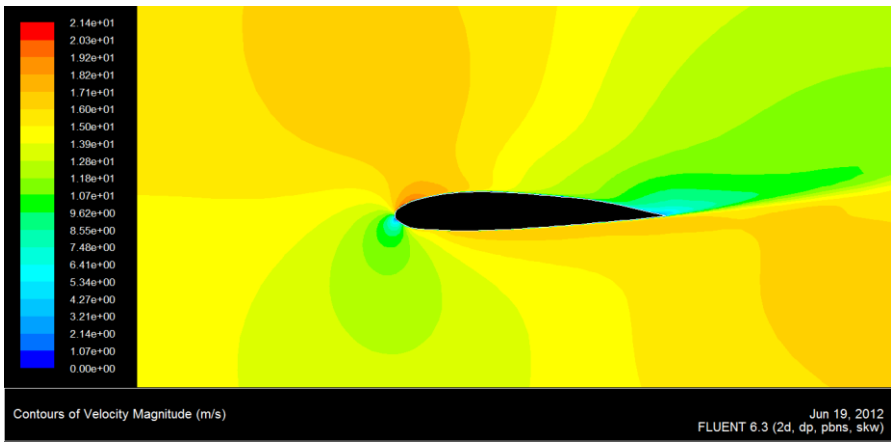

Figure 5.8 Pressure contour (18^0 Angle of attack and viscosity model k-ω)

5.5.2 Lift coefficient

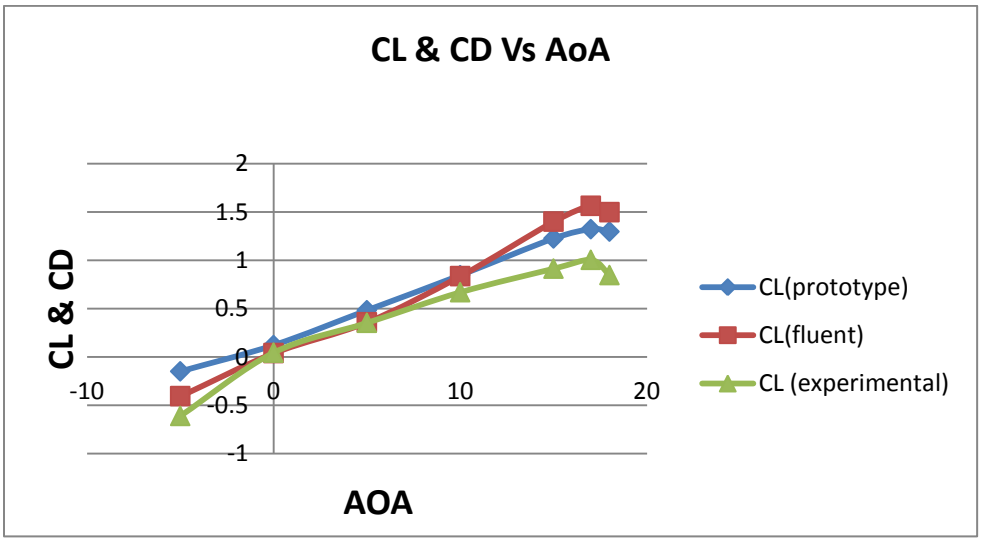

Figure 5.9 lift coefficient Vs Angle of Attack

5.5.3 Drag coefficient

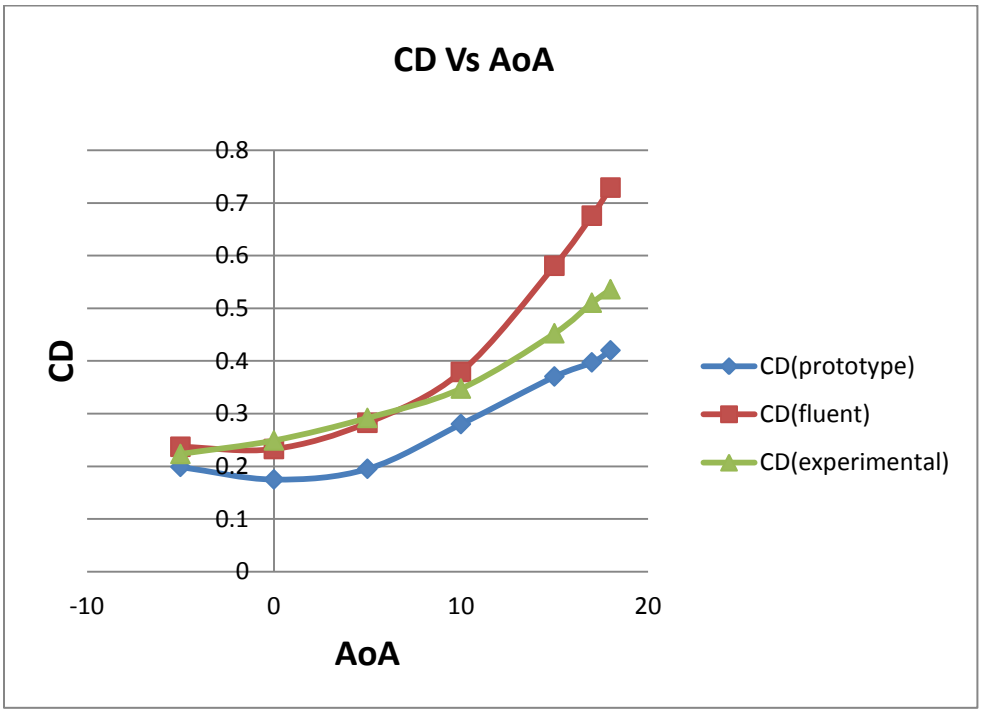

Figure 5.10 drag coefficient Vs Angle of Attack

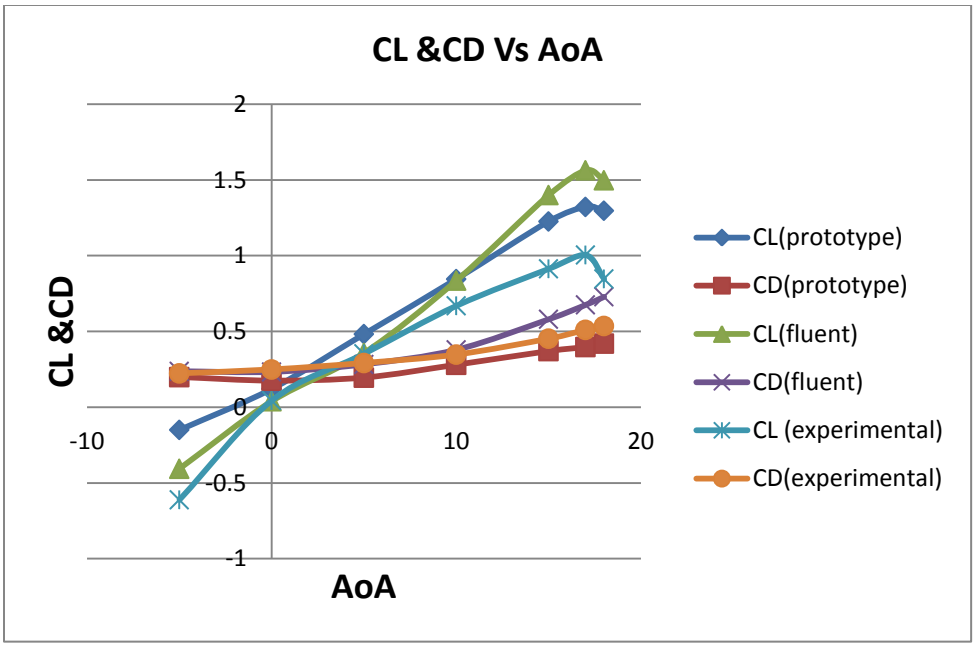

Figure 5.11 lift and drag coefficients Vs Angle of Attack

5.5.4 Lift and drag force

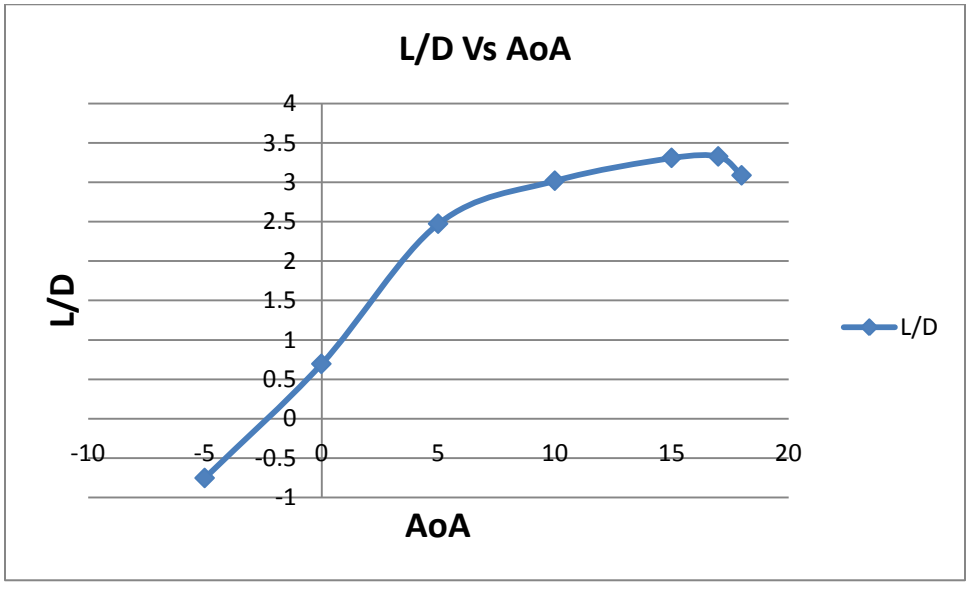

Figure 5.12 Lift to Drag (L/D) ratio Vs Angle of Attack

CHAPTER 6

CONCLUSION AND FUTURE SCOPE

6.1 Conclusion

In an aircraft, lift is caused by an upward force that is resulted from the difference in pressure between the top and the bottom surface of the wings. This difference in pressure is due to the special shape of the airfoil, and the amount of this lift is dependent upon the angle at which the wing is inclined.

To find the maximum performance of the wing, it should be tested in a wind tunnel at different angles of attack. From testing the NACA 2415 it is determined that the optimum angle of attack is between 15-17 degrees. Unfortunately, excessive drag is generated by the inaccuracies in the construction of the wing and the errors in the experiment.

Simulations have done on the different mesh ups and viscosity models. These simulations provide best approachable results to experimental data with quadrilateral map meshing of size 80×65 and k-ω as the viscosity model.

Lab experiment and CFD simulation has proven that for this particular NACA 2415 airfoil, the most effective angle of attack is at 17^0. From 4^0 to 17^0 the C_L will be increasing continuously and the ratio L/D will be over 1; within this range there will be effective use of the airfoil.

CFD simulation has been done on the prototype of the same model to analyze the results and concluded that results obtained are almost same.

6.2 Future scope

Good correlation between wind tunnel data and CFD simulations encourage that future modifications on airfoil design shall be investigated in simulation software. Though, it is emphasized that wind tunnel experiments must still be done to validate the accuracy of the evolving designs and computer models. Future work on the same subject acquires experimental data for more than one velocity.

RFERENCES AND BIBLIOGRAPHY

1. E.Guilmineau, J. Piquet & P. Queutey (1997) 2D turbulent viscous flow simulation past airfoils at fixed incidence. Comp. Fluids, Vol.26, pp.135-162.
2. Sunada, S., Sakaguchi, A., Kawachi, K.,Airfoil section characteristics at a low Reynolds number, Journal of Fluids Engineering, Vol.119,pp.129-135, 1997.
3. Lawson N, Wu J (1997) Three-dimensional particle image velocimetry: experimental error analysis of a digital angular stereoscopic system. Meas Sci Technol 8:1455–1464.
4. N. Ahmed, B.S. Yilbas*, M.O. Budair; Computational study into the flow field developed around a cascade of NACA 0012 airfoils. Comput. Methods Appl. Mech. Engrg. 167 (1998) 17-32.
5. T. K. Sen Gupta and K. Gupta; Effect of free-stream turbulence on flow over airfoil section at high incidence in march 2001; journal of fluids and structure dio:10.1006/jfls.2000.0373.
6. Kunz, P. J., Kroo, I.,Analysis, design and testing of airfoils for use at ultra-low Reynolds numbers, Proceedings of the Conference on Fised, Flapping and Rotary Vehicles at very Low Reynolds Numbers, edited by T. J. Mueller, Univ. of Notre Dame, Notre Dame, IN, pp.349-372, 2000.
7. Bouhadji and M.Braza; Organised modes and shock–vortex interaction in unsteady viscous transonic flows around an aerofoil Part II: Reynolds number effect in 2001; Computers & Fluids 32 (2003) 1261–1281
8. G. Wahba and Hafez; Optimal control of flow with discontinuities in 2002; Journal of Computational Physics 187 (2003) 660–682.
9. Sanjay Mittal and Priyank Saxena; Hysteresis in flow past a NACA 0012 airfoil. Department of Aerospace Engineering, Indian Institute of Technology, Kanpur, UP 208 016, India. Comput. Methods Appl. Mech. Engrg. 191 (2002) 2179–2189.
10. Marilyn J. Smith, Tin-Chee Wong, Mark Potsdam, James Baeder and Sujeet Phanse; Evaluation of CFD to Determine Two-Dimensional Airfoil Characteristics for Rotorcraft Applications. Presented at the American

Helicopter Society 60th Annual Forum, Baltimore, MD, June 7-10, 2004.Copyright © 2004 by the American Helicopter Society International, Inc. All rights reserved.

11. T. Nakanoa, N. Fujisawaa,_, Y. Ogumaa, Y. Takagia, S. Leeb; Experimental study on flow and noise characteristics of NACA0018 airfoil. Department of Mechanical Engineering, Niigata University, 8050 Ikarashi-2, Niigata 950-2181, Japan; Department of Mechanical Engineering, Inha University, 253 Yonghyun, Nam, Inchon 402-751, Korea. December 2006.
12. Y.C. Li, J.J. Wang *,1, J. Hua; Experimental investigations on the effects of divergent trailing edge and Gurney flaps on a supercritical airfoil. Fluid Mechanics Institute, Beijing University of Aeronautics and Astronautics, Beijing 100083, People's Republic of China. December 2006. Aerospace Science and Technology 11 (2007) 91–99.
13. Nitin R. Kapania, Katherine Terracciano and Shannon Taylor; modelling the fluid flow around the airfoils using conformal mapping in august 2008.
14. Zhu Jun, Gao Zhenghong, Zhan Hao, Bai Junqiang, A High-speed Nature Laminar Flow Airfoil and Its Experimental study in Wind Tunnel with Nonintrusive Measurement Technique in August 2008 ; Chinese Journal of Aeronautics 22(2009) 225-229
15. D. You and P.Moin; Active control of flow separation over an airfoil using synthetic jets in 2008; Journal of Fluids and Structures 24 (2008) 1349–1357.
16. Liu Z, Jia L, Zheng Y, Zhang Q (2008) Flow-adaptive data validationscheme in PIV. Chem Eng Sci 63:1–11.
17. Masoud Mirzaei, Mohammad A. Ardekani b, Mehdi Doosttalab; Numerical and experimental study of flow field characteristics of an iced airfoil. Aerospace Science and Technology 13 (2009) 267‑276.
18. R.W. Derksen and Tim Rogalsky, Bezier-PARSEC: An optimized aerofoil parameterization for design in October 2009; Advances in Engineering Software 41 (2010) 923–930.

19. D.N. Srinath, Sanjay Mittal, Optimal aerodynamic design of airfoils in unsteady viscous flows in February 2010 ; Computer Methods in Applied Mechanics and Engineering 199 (2010) 1976–1991.
20. S. Rajakumar, Dr.D.Ravindran; computational fluid dynamics Of windturbine blade at various Angles of attack and low Reynolds number. S.Rajakumar. et. al. / International Journal of Engineering Science and Technology Vol. 2(11), 2010, 6474-6484.
21. T. Nakanoa, N. Fujisawaa, Y. Ogumaa, Y. Takagia, S. Lee; Experimental study on flow and noise characteristics of NACA0018 airfoil in 2010; Journal of Wind Engineering and Industrial Aerodynamics 95 (2007) 511–531.
22. Kompenhans, J. Raffel, M. Dieterle, Lee, L. Dewhirst, T. Vollmers, H. Ehrenfried, K. Willert, C. Pengel, K. Kahler, C. Schroder, A. Ronneberger, 2000. Particle image velocimetry in aerodynamics; technology and applications in wind tunnels. J. Vis. 2, 229–244.
23. Alexander, Greg. NACA Airfoil Series. Aerospaceweb.org. http://www.aerospaceweb.org/question/airfoils/q0041.shtml
24. Aerodynamics of aircraft I, McGraw-Hill. (Excerpts from textbooks "Fundamentals of Aerodynamics", Fourth ed. & Introduction to flight, Fifth edition, both by *Anderson*)
25. Hermann Schlichting, Boundary-Layer Theory, chapter boundary layer control(suction/ blowing), pp. 291–321, Springer, 2000. And http://www.google.co.in/imghp?hl=en&tab=wi.
26. Sunada, S., Yasuda, T., Yasuda, K., Kawachi, K.,Comparison of wing characteristics at an ultralow Reynolds number, Journal of Aircraft, Vol.39, pp.331-338, 2002.